Structures 53 (2023) 1557–1581

Contents lists available at ScienceDirect

Structures

journal homepage: www.elsevier.com/locate/structures

Upgrading the hanger resistance of RC inverted T-girders using externally bonded carbon fiber reinforced polymers (EB-CFRP)

Ahmed M. Atta [a], Reda N. Behiry [a,*], Mohammed I. Haraz [b]

[a] Structural Engineering Dept., Faculty of Engineering, Tanta University, Tanta, Egypt
[b] Nile Higher Institute for Engineering and Technology, Mansoura, Egypt

ARTICLE INFO

Keywords:
Shear strengthening
Externally bonded carbon fiber reinforced polymers
Inverted T-girders
Hanger failure
And ductility

ABSTRACT

In modern bridges, inverted T-girders are considered the most popular structural solution for supporting longitudinal precast stringers. Nevertheless, they often experience a prevalence of cracking at the web-flange connection, leading to hanger failure. So, in many instances, such elements are in urgent need of being strengthened to keep up with the ongoing increases in traffic loads. Therefore, this paper investigates the effectiveness of externally bonded carbon fiber reinforced polymers for strengthening such girders. Eight third-scale specimens, including an un-strengthened reference one, were cast and tested under monotonic 4-point loading up to failure. Two arrangements were used, namely, continuous sheets (U-wrapped or side-bonded) and discontinuous strips. The sheet's height as well as the strip's centerline spacing were changed as key parameters. Based on the experimental results, it was mainly found that the externally bonded carbon fiber reinforced polymers strengthening technique was effective in increasing the hanger resistance and ductility of the inverted T-girders by roughly 1.37 and 1.42 times, respectively. Moreover, the initial stiffness and energy dissipation of the strengthened specimens were found to be considerably higher than the reference specimen by an average of 60% and 159%, respectively. In addition, by increasing the sheet's height from 200 to 400 mm, the contribution of the strengthening system to the hanger capacity was almost doubled. As for the strip's centerline spacing, it is advised that the strengthening strips be applied as close as possible to the loading locations because of the nonlinearity of their strain distribution. Finally, a model to predict the hanger capacities of the strengthened inverted T-girders was built and agreed well with the experimental capacities obtained during the tests, with an experimental-to-predicted ratio of 1.04 ± 0.03.

1. Introduction

Engineering society has widely recognized strengthening or rehabilitation as an urgent necessity to tackle the ageing of many reinforced concrete (RC) bridges. Due to economic and environmental constraints, it is safer, cheaper, and more practical to strengthen or repair existing concrete bridges than to completely demolish and rebuild them. Nowadays, strengthening of RC bridges has emerged in the construction community as an effective way to address a number of problems such as design errors, reinforcement corrosion, construction defects, and environmental harms. Also, in many countries, standards and codes are continually updated to keep pace with new loading requirements [1–3]. Accordingly, ACI 562–16 [4] classified the majority of the bridges that were designed in accordance with earlier codes as deficient structures in terms of strength and ductility. So, selecting the appropriate strengthening materials and techniques is still an ongoing interest for researchers and engineers.

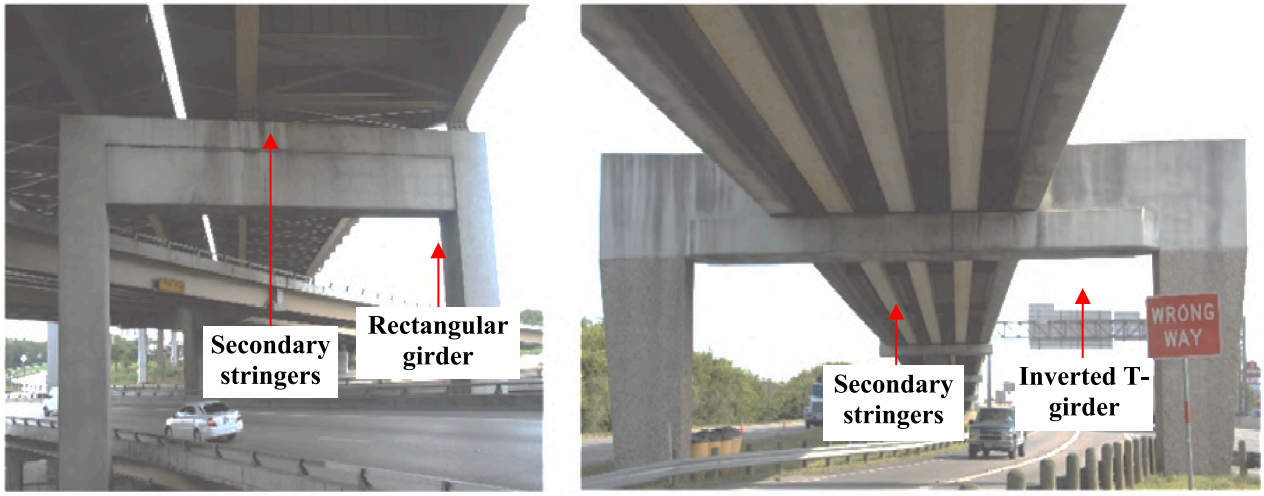
Different strengthening systems, such as concrete jacketing [5–10], steel jacketing [11–14], and external pre-stressing [15–18], have been suggested to improve the performance capacity of reinforced concrete structures. Recently, fiber reinforced polymers (FRP) have attracted more attention in the field of rehabilitation and repair works. Compared with the aforementioned strengthening materials, FRP appears to be the most applicable in terms of strength capacity, strength-to-weight ratio, corrosion resistance, ease of application, durability performance, and availability in a variety of types and shapes. In addition to their superior properties, FRP continuous sheets or discontinuous strips are bonded to the concrete surface onsite without specialized equipment to increase the strength of the member without causing a significant increase in external dimensions. So, this strengthening system has been extensively investigated for reinforced concrete elements in a series of experimental

* Corresponding author at: Structural Engineering Dept., Faculty of Engineering, Tanta University, Tanta 33511, Egypt.
E-mail address: Redabehiry@f-eng.tanta.edu.eg (R.N. Behiry).

https://doi.org/10.1016/j.istruc.2023.05.029
Received 5 December 2022; Received in revised form 15 April 2023; Accepted 7 May 2023
Available online 22 May 2023
2352-0124/© 2023 Institution of Structural Engineers. Published by Elsevier Ltd. All rights reserved.

Nomenclature

V_{sf}	Nominal shear friction resistance (N).
$f_c^{'}$	Concrete compressive strength for standard cylinder (MPa).
f_{yv}	Yield strength of shear reinforcement (MPa).
k_c	Fraction of concrete strength available to resist interface shear and equal to 0.25.
μ_f	Friction factor and equal to 1.40 for normal strength concrete placed monolithically.
A_{cv}	Area of concrete section resisting shear friction force (mm^2).
A_{vf}	Area of interface shear reinforcement crossing the shear plane within the area (mm^2).
a_v	Distance between the centroid of the loading plate and the edge of the web (mm).
V_{up}	Nominal punching shear resistance (N).
x	Distance between the edge of loading plate and the edge of web (mm).
w	Width of the loading plate (mm).
L	Length of loading plate in transverse direction perpendicular to the web (mm).
d_f	Distance between the centers of tension reinforcement to the bottom of the flange (mm).
V_u	Ultimate vertical load applied on the bottom flange (N).
N_u	Longitudinal forces perpendicular to the bottom flange axis (N).
$\varnothing$	Resistance factor and equal to 0.9 for flexure.
A_S	Area of tensile reinforcement (mm^2).
V_h	Nominal hanger resistance (N).
f_{yh}	Yield strength of hanger reinforcement (MPa).
A_{sh}	Area of hanger reinforcement (mm^2).
S_h	Spacing between hanger reinforcement (mm).
b_f	Width of the bottom flange (mm).
b	Width of the web (mm).
V_c	Hanger resistance produced by the concrete section (kN).
V_{sh}	Hanger resistance produced by the hanger reinforcement (kN).
V_f	Hanger resistance produced by the EB-CFRP sheets or strips (kN).
f_{fe}	Effective stress of the EB-CFRP sheets or strips (MPa).
A_f	Area of the EB-CFRP sheets or strips (mm^2).
S_f	Perpendicular center-to-center spacing of the EB-CFRP strips (mm).
W_f	Width of the EB-CFRP strip (mm).
t_f	Nominal thickness of the EB-CFRP sheet or strip (mm).
n_p	Number of CFRP plies.
λ	Normalized bond height.
h_{max}	Maximum bond height (mm).
h_e	Effective bond height (mm).
h_f	Height of the EB-CFRP sheet that is bonded to the web (mm).
n_f	Number of CFRP strips in hanger failure zone, which equals ($w + 2d_f$).
n_s	Number of vertical stirrups in hanger failure zone, which equals ($w + 2d_f$).



a. Traditional system b. Modern ITG system

Fig. 1. Comparison between the common structural systems of RC bridges [45].

[19–35], analytical [36–41], and numerical studies [42–44].

To this day, the transportation network continues to play a prominent role in most countries' economic growth. Bridges are considered the most important component in this network because they enhance mobility across regions and countries by providing quick and easy conveyance. In the past, conventional RC bridges were constructed by placing the secondary precast stringers on top of the main girders. These bridges appear to have less openness because of the substantial volume of the structural elements employed in this system. Moreover, traditional RC bridges involve additional construction and maintenance costs due to the intricate installation of their elements. Reinforced concrete inverted T-girders (ITGs) are one of the best-engineered structural methods for many current RC bridges. They increase the clearance height beneath the bridge while supporting the secondary RC precast stringers, lowering the overall construction cost [45]. A comparison of the above-mentioned structural systems used to construct RC bridges is

shown in Fig. 1.

Inverted-T girders have a more complex structural behavior than rectangular top-loaded girders because the loads are applied to the bottom flange rather than the top face of the web [46]. In a rectangular girder, the vertical reactions of the secondary stringers are applied to the top face of the web. Such vertical reactions cause distinct or a combination of two modes of failure, namely flexure and shear. In contrast, the behavior of RC inverted T-girders poses a challenge because of the complicated load transfer mechanism due to the stringers that are located on the top face of the bottom flange. The vertical reactions obtained from the stringers applied to the bottom flange flow in the transverse direction to the bottom of the web, next vertically to the top chord only through the vertical stirrup's reinforcement (hanger reinforcement), and lastly longitudinally to the supports at both ends of the RC inverted T-girder. As a consequence, RC inverted T-girders have the same two modes of failure as rectangular top-loaded girders plus four other modes of failure for the bottom flange that can be described as follows: (i) shear friction failure between the bottom flange and the web; (ii) punching shear failure of the flange under the loading point; (iii) flexure failure of the flange; and (iv) failure of the hanger reinforcement. Hanger failure is defined as the vertical separation between the bottom flange and the web around the top face of the bottom flange. The next section summarizes ITG's capacity for each failure mode.

2. Design formulas for inverted T-girders

The behavior of the bottom flange is one of the main challenges faced in the design of RC inverted T-girders, so the design equations that are used to estimate its capacities will be illustrated as follows and summarized in Table 1, in accordance with the empirical design approaches in the AASHTO LRFD Bridge Design Specification [47], the design provisions of ACI 318–19 [48], and the PCI Handbook [49]. It's worth mentioning that all variables stated in this paper are explained in the notation. Shear friction in an inverted T-girder occurs when there is sliding between the bottom flange and the web, as shown in Fig. 2.a. The flange's shear friction capacity (V_{sf}), which is presented in Row 1 of Table 1, is based on the width of the loading plate (w) and the distance between the centroid of the applied load point and the edge of the web (a_v). Referring to Fig. 2.b and the equations listed in Rows 2 and 3 of Table 1, the nominal punching shear capacity (V_{up}) depends on the distance (x) between edge of the loading plate and edge of the web.

The bottom flange bends because of stringer vertical and horizontal reactions, so tension reinforcement (A_s) at the top of the bottom flange must be included as shown in Row 4 of Table 1. This reinforcement, which is allowed to resist the flexural bending moment and axial forces, must be spread out over a distance of ($w + 5a_v$); see Fig. 2.c. The AASHTO LRFD Specification [47] demands that hanger reinforcement be provided to resist the tensile force generated due to the separation between the bottom flange and the web. For the ultimate limit state, the hanger capacity (V_h) is calculated as listed in Row 5 of Table 1. As sketched in Fig. 2.d, the contribution comes from the concrete section's resistance and hanger reinforcement (A_{sh}). It should be noted that none of the preceding design equations for inverted T-girders were applied to the strengthened girders.

3. Research significance

Recently, inverted T-girders (ITGs) have been considered one of the most important structural elements due to their frequent use in the construction of concrete bridges. Consequently, much of the previous research has focused on the study of their behavior. For instance, Mirza and Furlong [50] and Garber et al. [51] conducted experimental and analytical studies to examine the effect of different variables on the strength and serviceability of these bridges. At the end of their studies, it was concluded that the hanger reinforcement (stirrups) in ITGs contributes to both the sectional shear strength and the transfer of load from the flange to the compression chord within the girder. Existing RC inverted T-girders mostly need to be strengthened due to the fact that they were designed and constructed in accordance with out-of-date codes [52–55]. However, studies on ITGs' strengthening methods are scarce [56–59].

As a consequence, a suitable strengthening technique for these inverted T-girders has to be proposed in order to maintain the integrity of the entire structure and safe life as well. This paper attempts to determine the most effective arrangement and configuration of Externally Bonded Carbon Fiber Reinforced Polymers (EB-CFRP) to increase the hanger capacity of ITGs and, hence, magnify the benefit from strengthening. For this purpose, eight RC inverted T-girders were tested under static loading, and the efficiency of the proposed strengthening technique will be evaluated in terms of ultimate load capacity, initial stiffness, energy dissipation, and ductility index. Furthermore, a design formula based on the preceding design equations for inverted T-girders was established to consider the hanger capacity of the CFRP-strengthened ITGs.

Table 1
Design formulas for inverted T-girders [47–49].

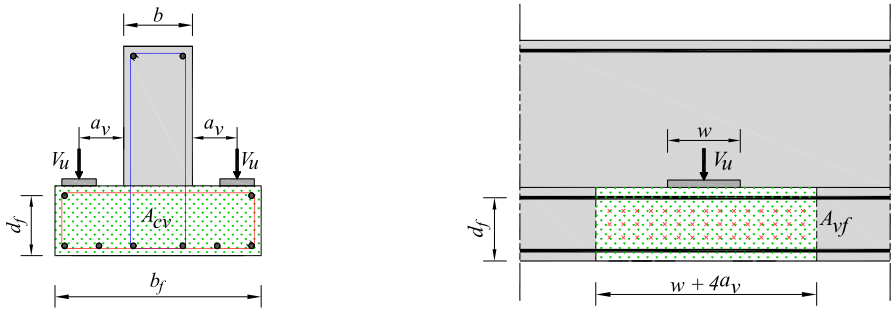
Row No.	Items	Formulas
(1)	Shear friction capacity	$V_{sf} = k_c A_{cv} f'_c + \mu_f A_{vf} f_{yv}$
(2)	Punching shear capacity	$V_{up} = 0.125\sqrt{f'_c}(w+2L+2d_f)d_f$ *for* $x \geq 0.50d_f$
(3)		$V_{up} = 0.125\sqrt{f'_c}(w+L+d_f)d_f$ *for* $x < 0.50d_f$
(4)	Flexure capacity	$A_s \geq \frac{2A_{vf}}{3} + \frac{N_u}{\varnothing f_y}$
(5)	Hanger capacity	$V_h = 0.17\sqrt{f'_c}b_f d_f + (\frac{w+2d_f}{S_h})f_{yh}A_{sh}$

4. Experimental work program

4.1. Geometry and reinforcement detailing

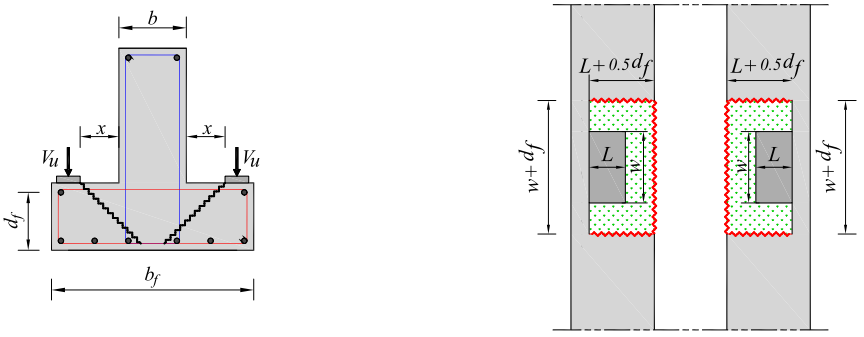
The experimental work program included eight tested specimens, each of which is a third-scale prototype for commonly used reinforced concrete inverted T-girders (ITGs). Seven specimens were strengthened with EB-CFRP, as well as one made as a reference specimen. By using AASHTO LRFD's formulas [47], the specimens were designed to avoid all expected types of failure (shear friction failure, punching shear failure under the point of loading, and flexure failure), excluding hanger failure. All the tested specimens were the same in terms of the concrete dimensions and the details of the reinforcing steel. The only difference was the way that EB-CFRP was set up in the hanger failure zone (mid-span zone).

In particular, the tested ITGs were simply supported over a span of 3000 mm center to center with a total height of 600 mm, a 200 mm web width, and a 600 mm flange width. To avoid the punching shear failure mechanism, a thickness of 200 mm was used for the bottom flange. The



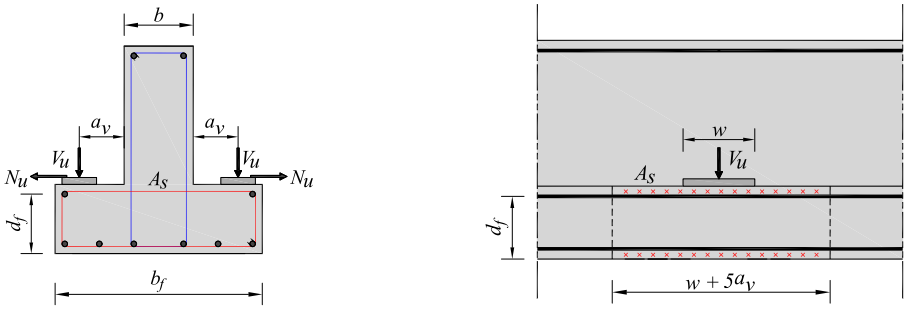
i. Cross section ii. Longitudinal section

a. Details for shear friction design



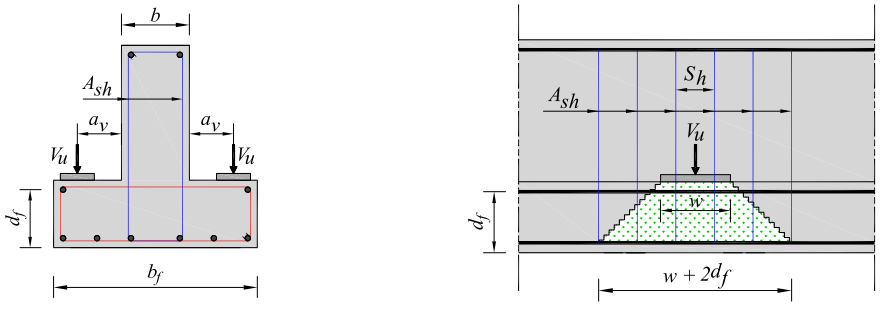
i. Cross section ii. Top view

b. Details for punching shear design



i. Cross section ii. Longitudinal section

c. Details for flexure design



i. Cross section ii. Longitudinal section

d. Details for hanger shear design

Fig. 2. Design sketches for ITGs based on recent standards [47–49].

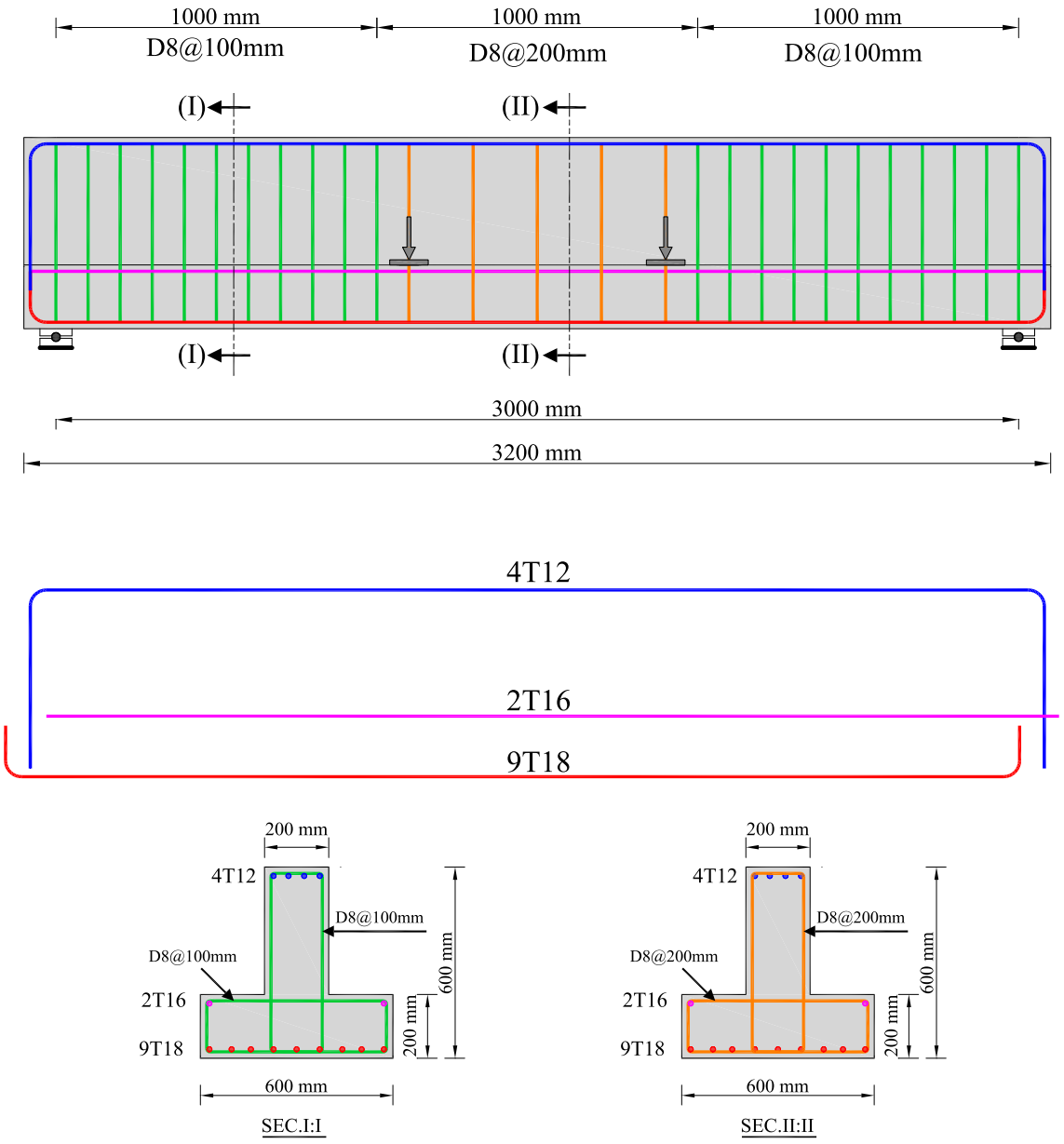


Fig. 3. Concrete dimensions and reinforcement details.

concrete cover was 25 mm for the web and 15 mm for the bottom flange. The amount and configuration of reinforcement were chosen to meet the minimum requirements of ACI 318–19 [48], regardless of how much was utilized to resist the hanger failure. Nine 18-mm deformed bars were arranged in one row as a lower reinforcement, while four 12-mm deformed bars were used as an upper reinforcement, and two 16-mm deformed bars were supplied in the top corner of the bottom flange to fix the transverse stirrups. Closed stirrups with a diameter of 8 mm spaced every 100 mm at the first and last meters behind the supports, were used to prevent the shear failure that could happen in the web.

Table 2
Specimen's description.

Group No.	Specimen No.	n_p	h_f (mm)	S_f (mm)	W_f (mm)	Configuration
Control	ITG-1	–	–	–	–	Reference girder
G1	ITG-2	Single	400	–	680	One continuous U-wrapped sheet (Single ply × 400 × 680 mm).
	ITG-3	Single	400	–	680	One continuous side-bonded sheet (Single ply × 400 × 680 mm).
G2	ITG-4	Single	300	–	680	One continuous side-bonded sheet (Single ply × 300 × 680 mm).
	ITG-5	Single	200	–	680	One continuous side-bonded sheet (Single ply × 200 × 680 mm).
G3	ITG-6	Double	400	283	113	Three discontinuous side-bonded strips (Double ply × 400 × 113 mm).
	ITG-7	Double	400	153	68	Five discontinuous side-bonded strips (Double ply × 400 × 68 mm).
	ITG-8	Double	400	105	49	Seven discontinuous side-bonded strips (Double ply × 400 × 49 mm).

n_p: Number of EB-CFRP plies, h_f: Height of EB-CFRP continuous sheet or discontinuous strip that bonded to the web, S_f: Spacing between the centerlines of CFRP strips, and W_f: Width of CFRP sheets/strips.

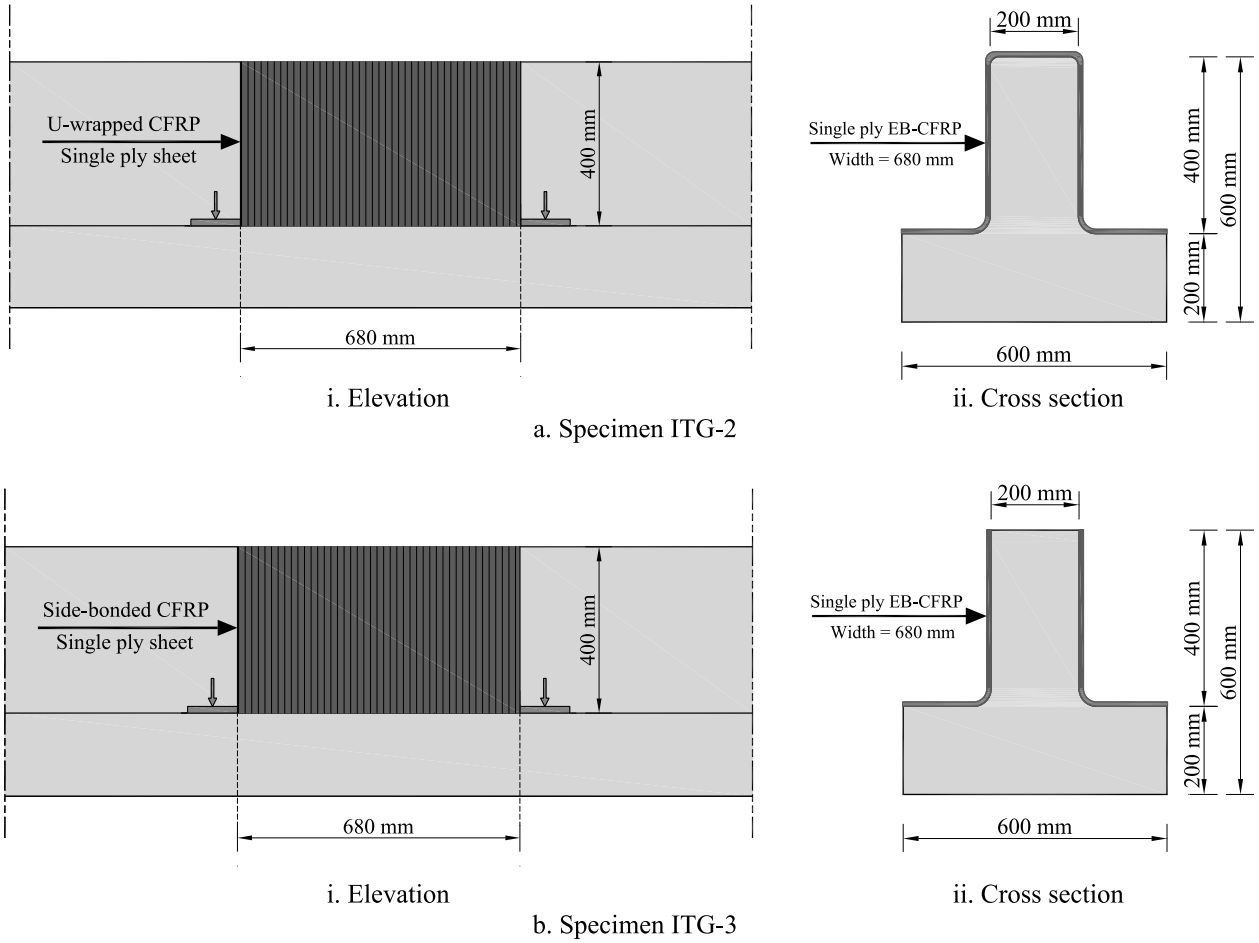


Fig. 4. Strengthening scheme for specimens in group (1).

However, the stirrups in the mid-span zone (hanger failure zone) were made of 8 mm diameter spaced every 200 mm. The concrete dimensions and reinforcement details for all tested reinforced concrete inverted T-girders are shown in Fig. 3.

4.2. Test inverted T-girders (ITGs)

As shown in Table 2, eight ITGs, divided into three groups, as well as a control specimen, were investigated through a series of tests until hanger failure occurred. The purpose of this test was to determine the efficacy of the EB-CFRP strengthening system in enhancing the hanger capacity. The specimen ITG-1 was an un-strengthened RC inverted T-girder, which acts as a reference. Group No. 1 included two specimens strengthened using a single ply of EB-CFRP continuous sheet in two different configurations: U-wrapped (ITG-2) or side-bonded (ITG-3). Referring to Fig. 4, all EB-CFRP sheets were positioned along the studied region between the applied loads and had a width of 680 mm. In the second group, the continuous EB-CFRP sheet was constant in both width (680 mm) and number of plies (single ply only), while the heights (h_f) of the EB-CFRP sheet that bonded to the web were varied. The specimens ITG-3, ITG-4, and ITG-5 were strengthened with EB-CFRP's heights of 400 mm, 300 mm, and 200 mm, respectively, as shown in Fig. 5. In the last group, EB-CFRPs in the form of discontinuous strips with varied spacing were used to strengthen the inverted T-girders. In detail, the specimens ITG-6, ITG-7, and ITG-8 were strengthened by double ply EB-CFRP strips, one over the other. Each strip started from the top of the specimen web and extended over the upper face of the bottom flange. The widths of the EB-CFRP strips for specimens ITG-6, ITG-7, and ITG-8 were 113 mm, 68 mm, and 49 mm, respectively, while the spacing between their center lines was equal to 283 mm, 153 mm, and 105 mm, respectively, as shown in Fig. 6. Certainly, for comparison purposes, the total cross-sectional area of EB-CFRP sheets or strips in all strengthened ITGs was almost kept constant.

4.3. Material properties

In plywood formworks, all test specimens were simultaneously cast, and they were cured with wet burlap. Ready-mixed concrete was used, containing 1040 kg/m^3 crushed limestone aggregate with a maximum size of 20 mm, 760 kg/m^3 natural sand, 400 kg/m^3 Ordinary Portland Cement (Type I), and 160 kg/m^3 water. The ASTM standard [60] was used to determine the compressive strength of the used concrete. The standard cylinders with dimensions of 150 mm in diameter and 300 mm in height were tested after 28 days on the same day as the ITG specimens. The compressive strengths were 30.1, 32.4, 31.5, 30.3, 28.1, 31.4, 32.2, and 30.2 MPa for specimens ITG-1, ITG-2, ITG-3, ITG-4, ITG-5, ITG-6, ITG-7, and ITG-8, respectively. By analyzing this data, it can be concluded that the average compressive strength was 30.8 MPa with a standard deviation of 1.40 MPa and a coefficient of variation of 4.55%. Stirrup and longitudinal reinforcement were formed using steel bars with diameters of 8, 12, 16, and 18 mm. Three samples of each diameter were tested according to ASTM A615/A615M [61] using a universal testing machine with a capacity of 200 kN and a loading rate of 0.1 mm/s. For bars with a diameter of 8, 12, 16, and 18 mm, the tensile yield strengths were 245, 440, 435, and 410 MPa, respectively, whereas the corresponding ultimate values were 365, 625, 620, and 600 MPa. The dry unidirectional carbon fibers that were used to strengthen ITGs were SikaWrap-600C, and its epoxy resin was Sikadur-330. According to the

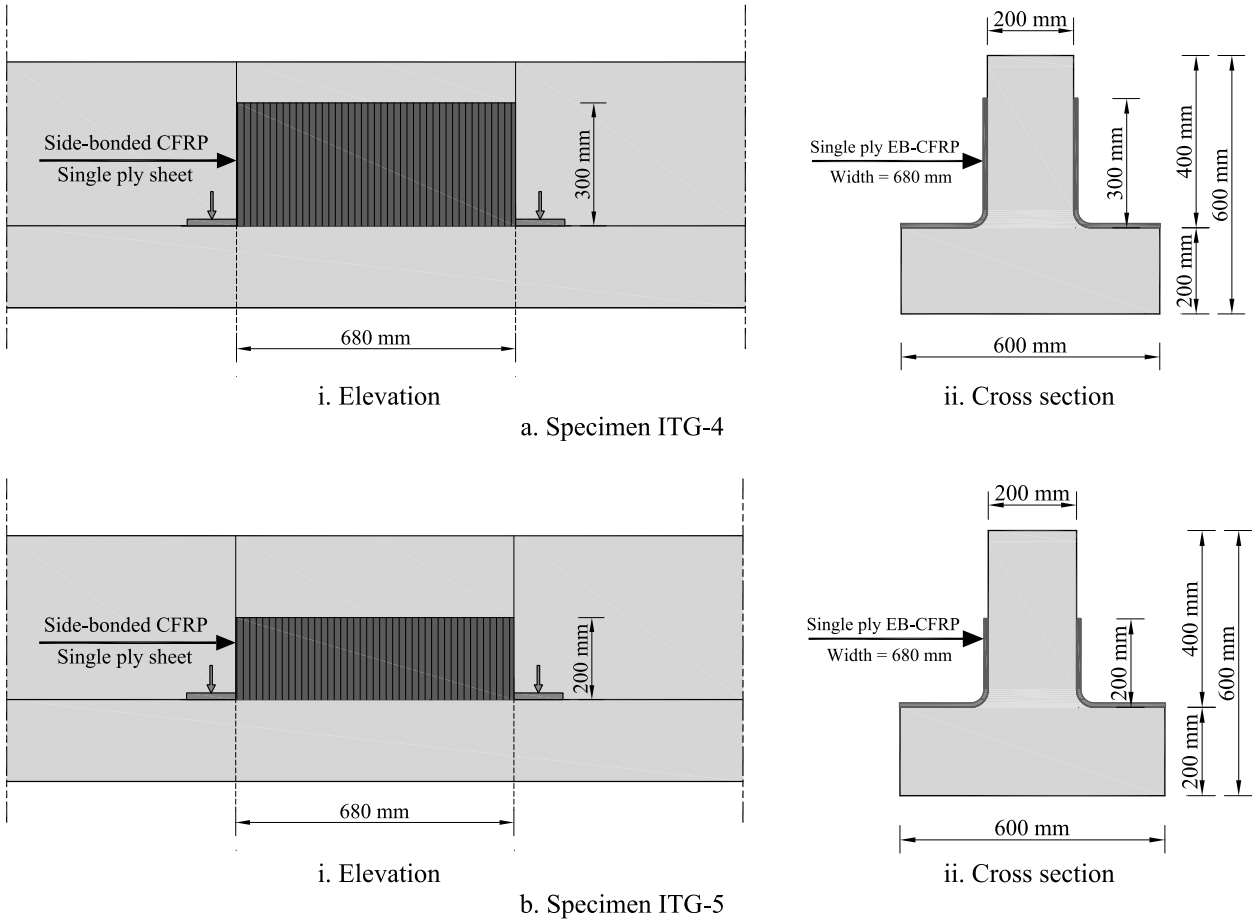


Fig. 5. Strengthening scheme for specimens in group (2).

manufacturer's data sheets [62], dry unidirectional carbon fibers have a thickness of 0.331 mm, a tensile strength (f_f) of 3800 MPa, an elastic modulus of 242 GPa, and an elongation of 1.43%.

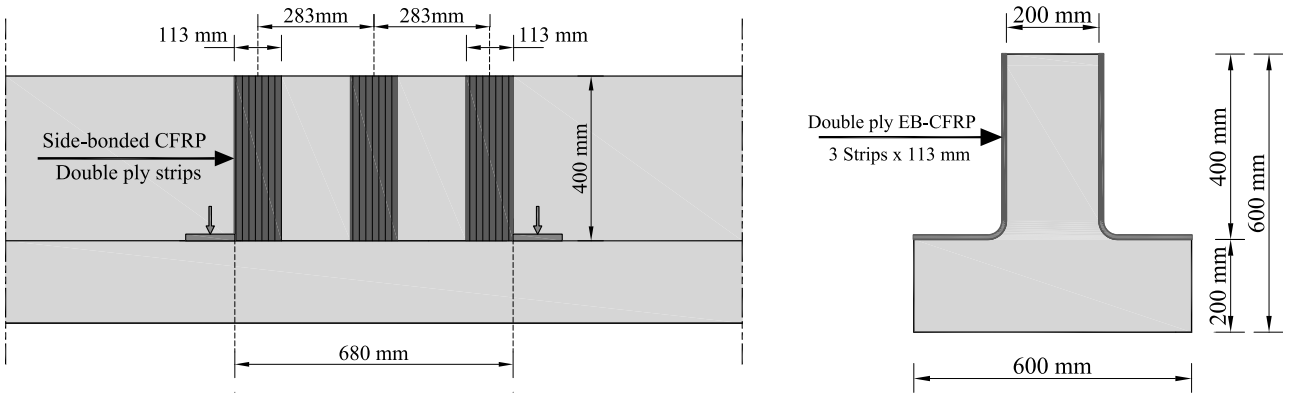
4.4. Strengthening procedure

One of the eight inverted T-girders (ITGs) produced was chosen as a reference (ITG-1), and the other seven (ITG-2 to ITG-8) were strengthened with different EB-CFRP arrangements and configurations. Dry unidirectional carbon fiber fabric in a 90° arrangement with a density of 600 g/m^2 was utilized to strengthen ITGs. Prior to the installation of the EB-CFRP system, the following steps were taken to strengthen ITGs: 1) grinding the concrete surface to remove cement laitance, loose, and friable materials using a hand grinder where EB-CFRPs were to be bonded; 2) cleaning the surface using an air compressor to remove dust that would weaken adhesion over time; 3) rounding the two corners at the top of the web to a minimum radius of 25 mm in order to avoid stress concentration at EB-CFRPs; this step was taken for the U-wrapped system only, as done in specimen ITG-2; and 4) at the connection between the web and the bottom flange, a concave epoxy mortar with a radius of 50 mm was used in order to reduce the stress concentration in the EB-CFRPs.

To bond the CFRPs, two components, resin (A) and hardener (B), were mixed in a ratio of 4:1 by weight with the recommendation of the manufacturer [62] by using a mixing spindle connected to a slow-speed electric drill (300 rpm) until the substance became smooth, inconsistent, and uniformly grey in color. Then, a thin layer of a two-component epoxy resin was applied to the concrete surface as a first coat. Finally, CFRPs were impregnated with the same epoxy resin and bonded to the concrete surface. During the installation of the EB-CFRP system, a roller was used to guarantee full saturation and remove any entrapped air bubbles. Definitely, the installation of the EB-CFRP system was performed as shown in Fig. 7 in accordance with the manufacturer's instructions and the specifications of ACI 440.2R-08 [63].

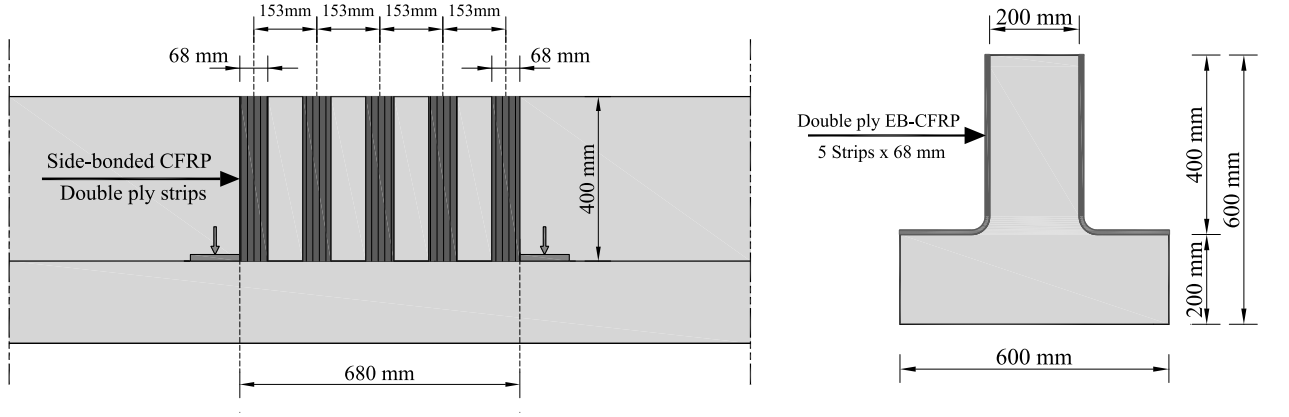
4.5. Test setup and instruments

All simply supported inverted T-girders (ITGs) were tested using a four-point loading protocol, as shown in Fig. 8. The span of the specimen was 3000 mm, and the distance between the centerlines of the loading plates was 800 mm. A hydraulic jack with a 1000 kN capacity was used to gradually apply the load up to failure. A special rigid steel frame was designed and manufactured to distribute the jack load into four equal square steel pads (length = 120 mm and thickness = 25 mm). The vertical deflections at the mid-span and beneath each loading point were measured using five linear variable differential transducers (LVDTs) with a measuring length of 100 mm. Furthermore, two LVDTs were also placed above the supporting points to measure the net-deflection of the test specimens. Electrical strain gauges were mounted on the lower tension mid-steel bar, the hanger stirrup in the mid-span, and the EB-CFRP sheets/strips. It is worth mentioning that the strain gauges for hanger stirrups and EB-CFRPs were fixed at the intersection between the expected crack path and the vertical centerlines of stirrup legs or EB-CFRPs, see Fig. 9. Moreover, a Pi-gauge was installed on the compression zone in the mid-span section to monitor the compressive strain in the concrete. After each loading step, a data acquisition system (TDS-150) automatically recorded and saved the failure loads, vertical displacements, and strains.



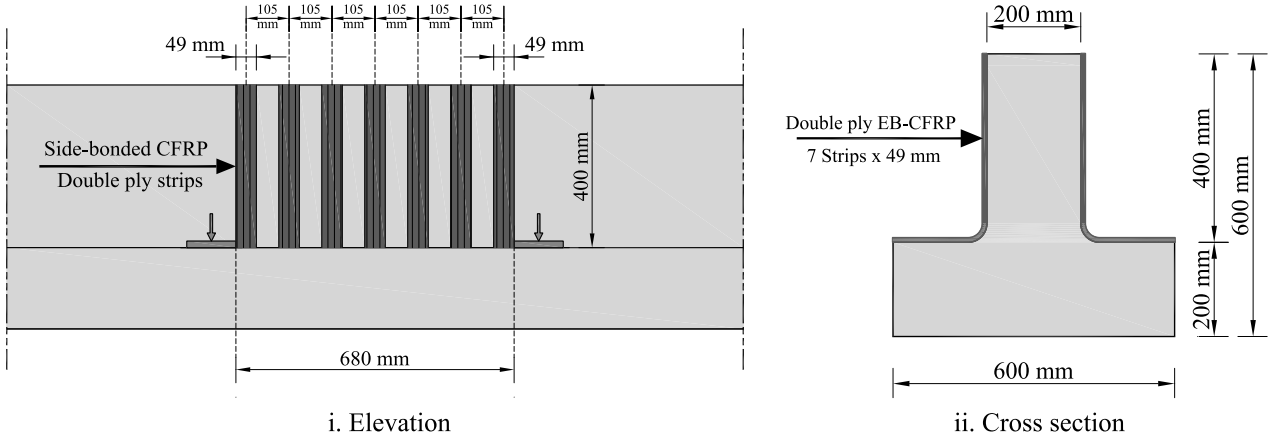
i. Elevation ii. Cross section

a. Specimen ITG-6



i. Elevation ii. Cross section

b. Specimen ITG-7



i. Elevation ii. Cross section

c. Specimen ITG-8

Fig. 6. Strengthening scheme for specimens in group (3).



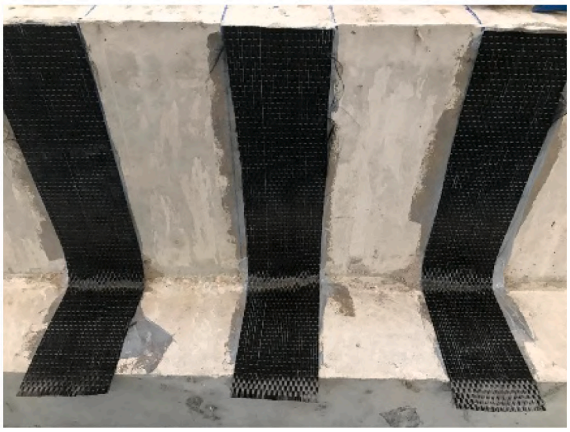
a. Grinding and cleaning the concrete surface.



b. Rounding and filleting web-flange connection.



c. Applying epoxy resin to the concrete surface



d. Applying CFRPs to concrete surface

Fig. 7. The installation process of EB-CFRP system.

5. Experimental results

The results of the experimental tests performed on the control and strengthened inverted T-girders (ITGs) are shown in Table 3. The discussion of failure modes, cracking, and ultimate loads is covered in Sections 4.1 and 4.2, respectively, while Sections 4.3 and 4.4 focus on the effectiveness of the EB-CFRP system and its deformational characteristics (load–deflection response, initial stiffness, energy dissipation, and ductility). In Section 4.5, the load–strain relationships are finally shown.

5.1. Failure modes

The crack patterns of all tested ITGs, whether they were strengthened or not (control), are depicted in Fig. 10.a through 10.h, shortly prior to the failure. As anticipated, all tested ITGs failed in the hanger mechanism, even with the existence of EB-CFRP strengthening. Consequently, no shear friction, punching shear, or flexure failures were observed for the bottom flange of any tested specimen. Regarding the control specimen (ITG-1), the first flexural cracks occurred within the mid-span at a load equal to 96 kN, which represents 20.0% of the ultimate load (P_u = 482.1 kN). In order to transition the applied load from the bottom flange to the top of the web and then to the supports, vertical tension forces were generated in the web. When these tension forces exceed the maximum tensile force of concrete, a horizontal crack appears in the connection between the web and the bottom flange. The first visible horizontal crack appeared at a load of about 379.2 kN (78.7% P_u). As the load increased, the horizontal crack widened; then, diagonal cracks appeared near the point of loading and then extended in an arched manner to the mid-height of the web, as shown in Fig. 10.a.

Obviously, due to the presence of CFRP systems, the cracks at earlier stages were not observed, so the first hanger cracking loads are estimated from the strain analysis of hanger stirrups. As shown in Fig. 10, the final dominant failure modes for the CFRP-strengthened specimens ITG-2, ITG-3, ITG-4, and ITG-5 were debonding between the CFRP sheets and the substrate concrete, followed by a sudden breakdown between the bottom flange and the vertical web. While, for strengthened specimens with CFRP strips (ITG-6, ITG-7, and ITG-8), the mode of failure was governed by delamination followed by a sudden separation of the concrete cover of the bottom flange. After the complete debonding or delamination of most CFRP, the specimens showed rapid development of cracking and deformation as the load was further increased. Another observation from the experimental test of the strengthened specimen with a U-wrapped CFRP sheet (ITG-2) is that no local rupture at the top corners of the web was observed as these corners were well-rounded. It is worth mentioning that the load at complete debonding of the most highly stressed CFRPs is defined in this study as the debonding load (P_d). Additionally, it was difficult to estimate the debonding loads experimentally; as a result, the debonding loads were approximately estimated based on the audible noise produced during the debonding process. Table 3 shows that the debonding loads of the strengthened specimens were about 88% of their ultimate loads.

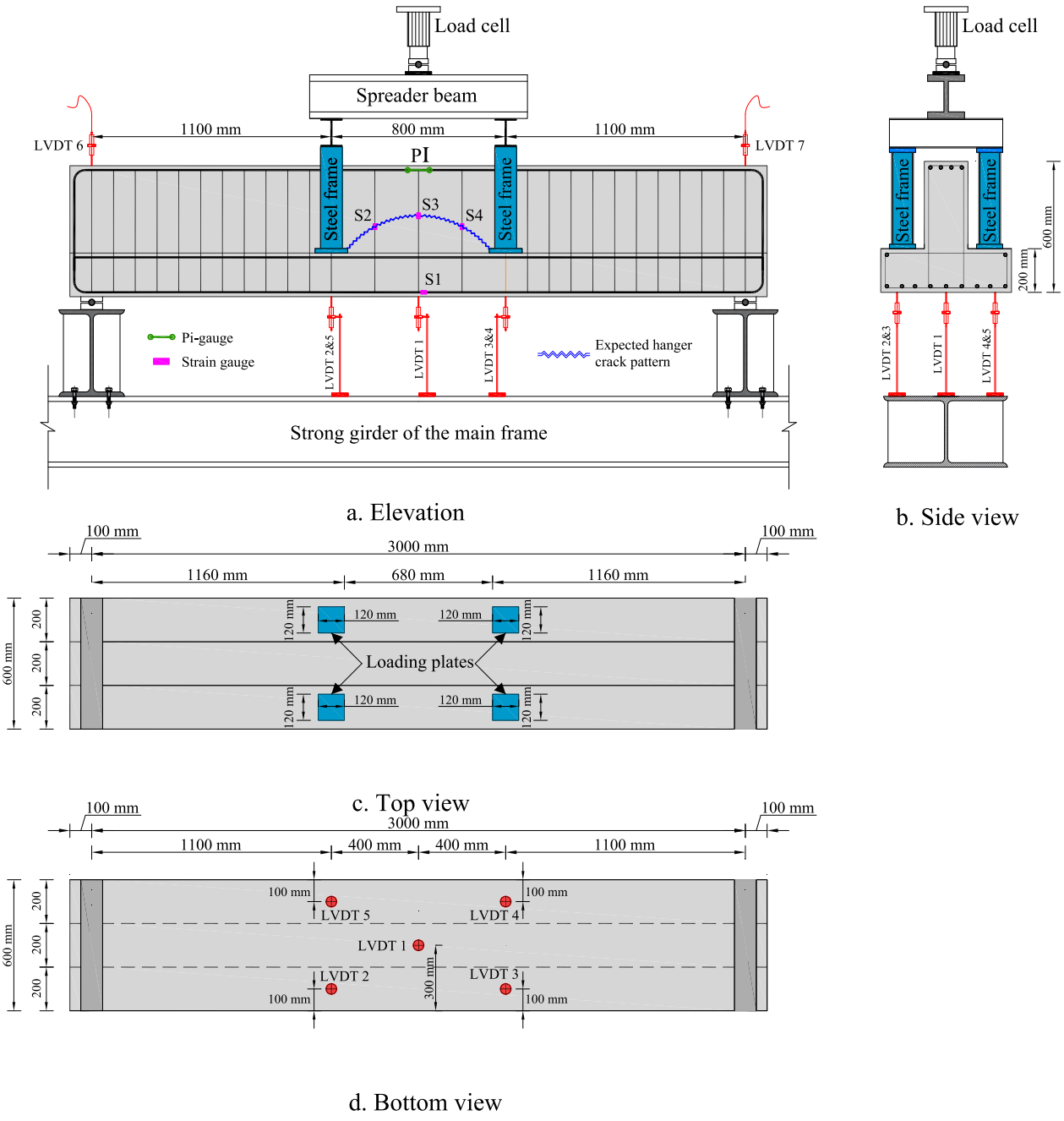


Fig. 8. Test setup and instrumentations.

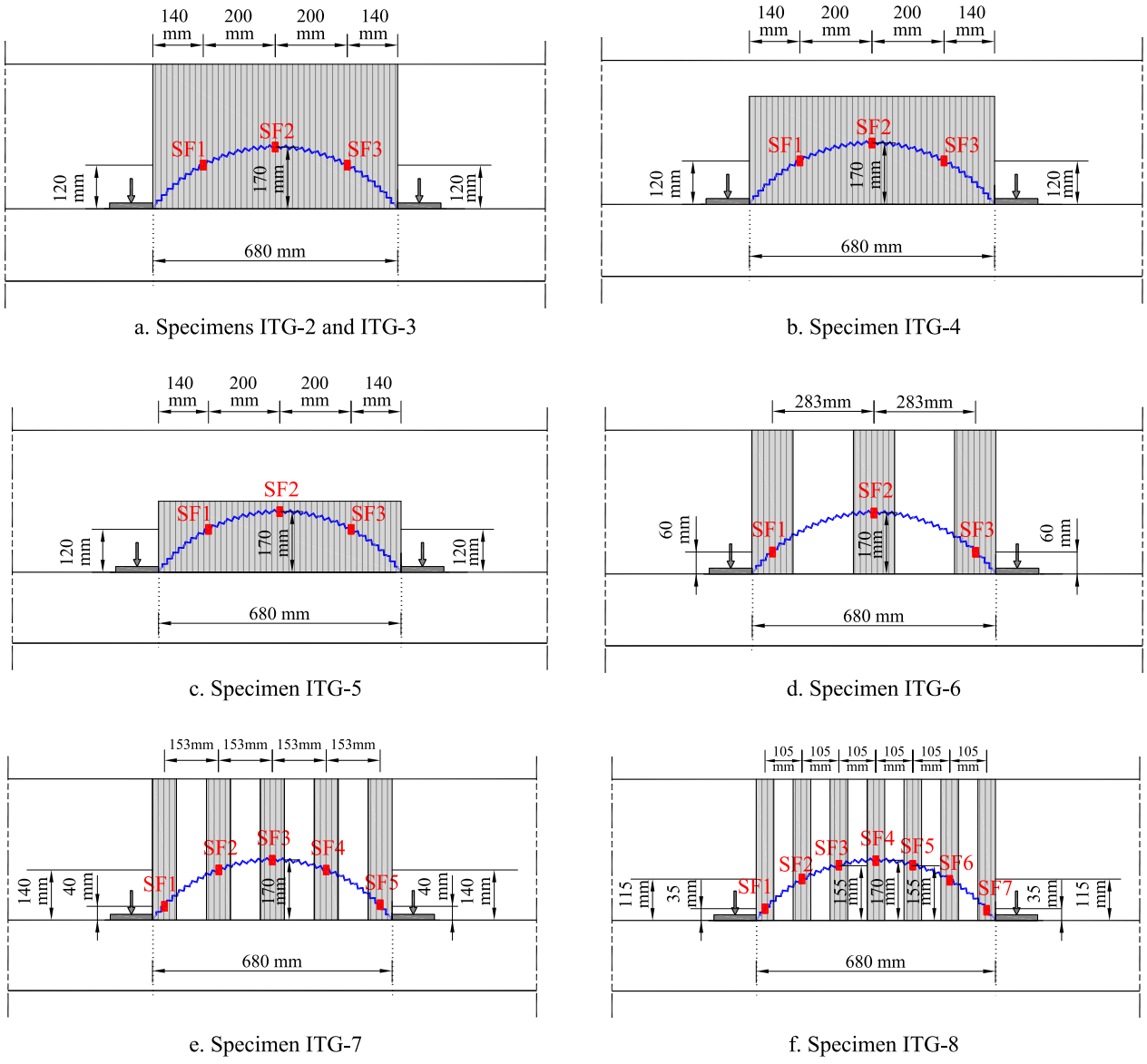


Fig. 9. Location of strain gauges that attached on CFRPs.

5.2. *Cracking and ultimate loads*

The cracking (P_{cr}), debonding (P_d), and ultimate (P_u) loads for all strengthened ITGs as well as the reference specimen are summarized in Columns 1, 2, and 3 of Table 3. Concerning the results of the cracking loads, the increases in cracking capacity for strengthened specimens are insignificant; the average increase is 3% compared to the un-strengthened specimen (ITG-1). These results confirm that the proposed EB-CFRP system does not contribute to the cracking stage, and the concrete section is only responsible for transmitting the loads applied at the bottom flange to the web. It is worth mentioning that the cracking load of the un-strengthened specimen was recorded when the first horizontal crack appeared. However, for strengthened ITGs, these loads are computed from the load–strain relationships of hanger stirrups. At the first crack performed, a jump in the tensile strain of hanger stirrups was recorded. For example, the cracking load of the strengthened specimen ITG-2 is 392.9 kN, in which the tensile strain in hanger stirrups was 198 με before cracking and jumped to 644 με just after cracks appeared.

To talk about how the EB-CFRP system strengthens RC inverted T-girders, the gains in ultimate loads for the strengthened ITGs are calculated with respect to the reference specimen and listed in Column 4 of Table 2. It can be concluded that the overall respective gains in ultimate load capacity for strengthened ITGs were a minimum of 16% and a maximum of 65% relative to the un-strengthened specimen (ITG-1). With regard to EB-CFRP configurations (U-wrapped or side-bonded), ITG-2 strengthened with U-wrapped EB-CFRP showed a higher

Table 3
Test results.

Specimen No.	Loads						Deflections		Initial stiffness		Energy dissipation				Ductility index		Strains		
	(1)	(2)	(3)	(4)	(5)	(6)	(7)	(8)	(9)	(10)	(11)	(12)	(13)	(14)	(15)	(16)	(17)	(18)	(19)
	P_{cr} (kN)	P_d (kN)	P_u (kN)	Gain %	P_f (kN)	ψ_f	δ_y (mm)	δ_{max} (mm)	k_i (kN/mm)	Gain %	E_y (kN.mm)	E_{max} (kN.mm)	$\mu_E\left(\frac{E_{max}}{E_y}\right)$	Gain %	$\mu_D\left(\frac{\delta_{max}}{\delta_y}\right)$	Gain %	ε_{cmax} ($\mu\varepsilon$)	ε_{smax} ($\mu\varepsilon$)	ε_{hmax} ($\mu\varepsilon$)
ITG-1	379.2	–	482.1	–	–	–	7.09	11.34	68.7	–	1732	3604	2.08	–	1.60	–	1007	805	3342
ITG-2	392.9	601.1	680.9	41%	198.8	47%	7.75	19.03	119.4	74%	2829	10,012	3.54	70%	2.46	54%	2109	1497	5447
ITG-3	387.1	572.0	655.6	36%	173.5	41%	7.71	18.27	113.6	65%	2898	9825	3.39	63%	2.37	48%	2074	1471	4364
ITG-4	385.7	552.7	639.3	33%	157.2	37%	8.64	16.33	87.1	27%	2647	7344	2.77	33%	1.89	18%	1854	1386	3851
ITG-5	381.3	486.4	559.5	16%	77.4	18%	9.32	16.61	73.9	8%	2583	6537	2.53	22%	1.78	11%	1369	1139	3618
ITG-6	402.1	699.6	795.5	65%	313.4	74%	7.43	21.11	153.8	124%	3093	13,125	4.24	104%	2.84	78%	2712	1819	5901
ITG-7	398.0	618.3	702.2	46%	220.1	52%	7.22	19.15	130.2	90%	3087	11,199	3.63	75%	2.65	66%	2285	1564	5381
ITG-8	385.5	551.2	603.0	25%	120.9	29%	8.58	16.59	92.6	35%	2810	7339	2.61	25%	1.93	21%	1638	1299	4932

Where, Column (1): P_{cr} is the hanger cracking load, Column (2): P_d is the debonding load, Column (3): P_u is the ultimate load, Column (4): is the gain in the hanger capacity corresponding to control specimen (ITG-1), Column (5): P_f is the hanger resistance of EB-CFRPs, Column (6): (ψ_f) is the CFRP's efficiency ratio, Column (7): δ_y is the deflection corresponding to the yielding load, Column (8): δ_{max} is the maximum deflection corresponding to the 85% P_u after peak point, Column (9): k_i is the initial stiffness, Column (10): the gain in the initial stiffness corresponding to control specimen (ITG-1), Column (11): E_y is the elastic energy dissipation corresponding to the yielding load, Column (12): E_{max} is the total energy dissipation corresponding to 85% P_u after the peak load, Column (13): μ_E is the energy dissipation index, Column (14): the gain in the energy dissipation corresponding to control specimen (ITG-1), Column (15): μ_D is ductility index, Column (16): the gain in the ductility index corresponding to control specimen (ITG-1), Column (17): ε_{cmax} is the compressive strain in concrete corresponding to the ultimate load, Column (18): ε_{smax} is the tensile strain in flexural reinforcement corresponding to the ultimate load, Column (19): ε_{hmax} is the tensile strain in hanger stirrups corresponding to the ultimate load.

increase in ultimate load capacity than that of the side-bonded scheme by 5%. This insignificance increases as the location of debonding occurs near the connection between the web and the bottom flange, so there is no need to use the U-wrapped configuration for strengthening RC inverted T-girders.

As far as EB-CFRP bonded height is concerned, the ultimate hanger capacity for strengthened ITGs was enhanced by increasing the height of the EB-CFRP sheet that was bonded to the web. In more details, specimens ITG-3, ITG-4, and ITG-5 with EB-CFRP heights (h_f) of 400 mm, 300 mm, and 200 mm, respectively, failed at an ultimate load of 655.6 kN, 639.3 kN, and 559.5 kN, which yields a gain in ultimate load capacity of about 36%, 33%, and 16%, respectively. In group (3), which studies the effect of spacing between centerlines of EB-CFRP strips, the gains in ultimate load were 65%, 46%, and 25% for specimens ITG-6 ($S_f = 283$ mm), ITG-7 ($S_f = 153$ mm), and ITG-8 ($S_f = 105$ mm), respectively. This observation emphasizes the pronounced connotation of applying the EB-CFRP strengthening system as close as possible to the loading plates of ITGs. It is worth mentioning that, as shown in Fig. 11.a and 11.b, the relationship between ultimate load capacity and EB-CFRP heights (h_f) or spacings (S_f) was not linear.

5.3. The EB-CFRP system's efficiency

The hanger capacity of the strengthened ITGs was higher than that of the control specimen, even though the EB-CFRP system did not reach its maximum tensile strength (P_t) as the predominant failure mode was debonding. So, from the perspective of strengthening efficiency, the CFRP efficiency ratio (ψ_f) was calculated for each strengthened specimen as listed in Column 6 of Table 3. The efficiency ratio is defined as the contribution of CFRPs to hanger resistance (P_f) divided by the tensile strength of CFRPs ($f_t = 3800$ MPa, and therefore $P_t = 423$ kN). Based on the simple superposition rule, the hanger capacity is the sum of three contributions: (i) the concrete contribution (P_c), (ii) the hanger reinforcement contribution (P_{sh}), and (iii) the contribution of the EB-CFRP system (P_f). The part of ($P_c + P_{sh}$) was assumed to be the hanger contribution of the control specimen (ITG-1) at the ultimate state. So, the contribution of EB-CFRP system ($P_f = P_u - [P_c + P_{sh}]$) can be considered experimentally as the difference value between the ultimate load (P_u) of a strengthened specimen and that of the control specimen ($P_c + P_{sh}$).

The CFRP efficiency ratio is almost equal for both configuration systems, U-wrapped and side-bonded. This shows that the side-bonded configuration is a good way to strengthen ITGs because it is easy to install and use. Regarding EB-CFRP bonded height, the efficiency ratios were 41%, 37%, and 18 % for specimens ITG-3 ($h_f = 400$ mm), ITG-4 ($h_f = 300$ mm), and ITG-5 ($h_f = 200$ mm), respectively. Although specimens ITG-6 (three strips) and ITG-8 (seven strips) had the same total cross-sectional area of CFRP material, the efficiency ratio was 74% for ITG-6 versus 29% for ITG-8. Consequently, to achieve the best use of the adopted strengthening technique, it can be advised to use EB-CFRP strips as close as possible to the loading points. It is worth noting that these efficiency ratios are only valid for the CFRP-strengthened ITGs that were subjected to concentrated loads. Otherwise, the contribution of the CFRP composites and thus their efficiency ratios may differ if the ITGs were exposed to distributed loads, owing to the change in the mechanism of load transfer in such case.

5.4. Deformational characteristics

5.4.1. Load-deflection response

Fig. 12.a through 12.c display the net load–deflection relationships of the control and strengthened ITGs. In general, the proposed strengthening method (EB-CFRP) led to a noticeable improvement in the response to deflection, initial stiffness, and ductility of the strengthened ITGs. The relationship between the applied load and the associated net deflection for all tested ITGs, with and without strengthening, is almost

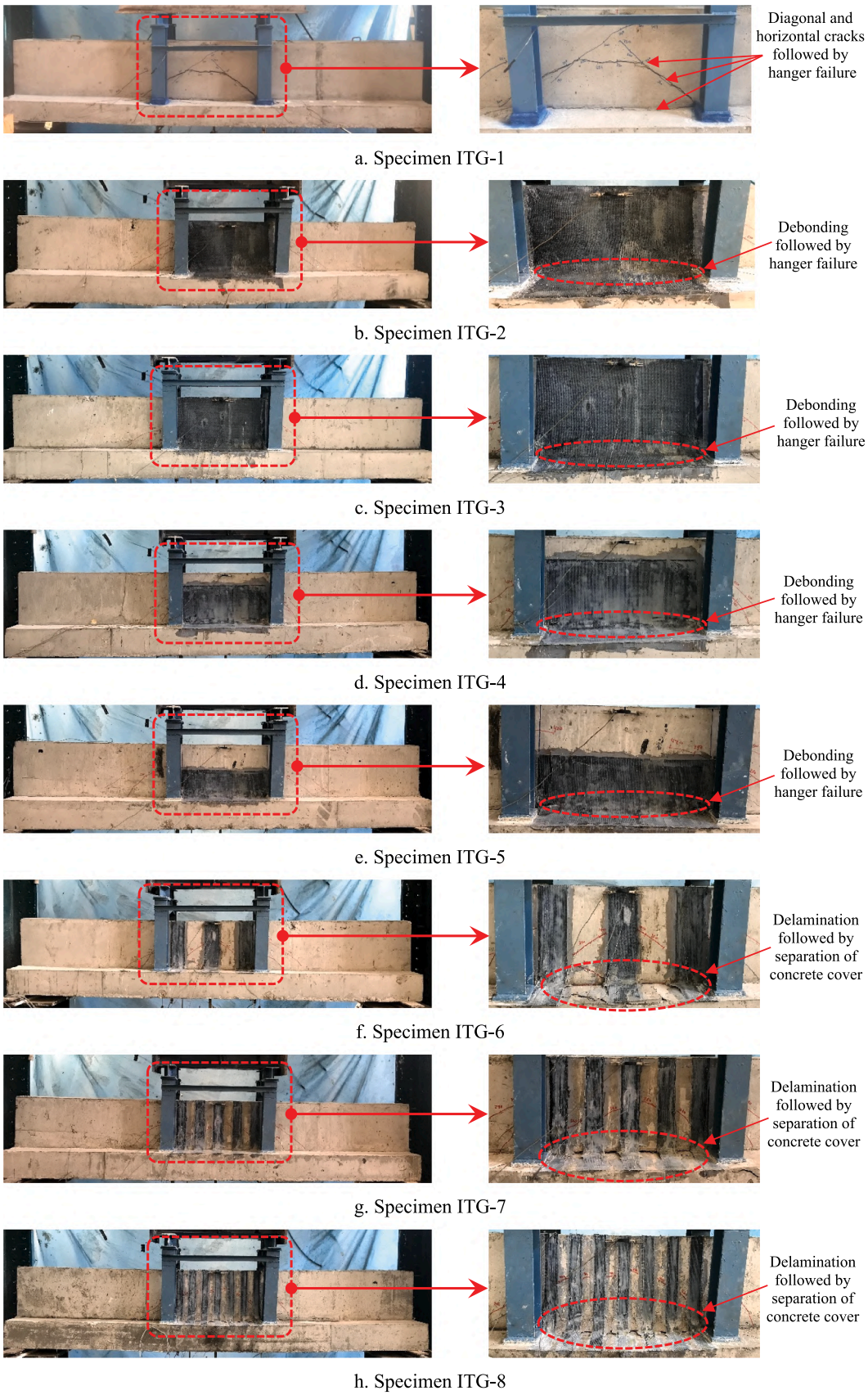
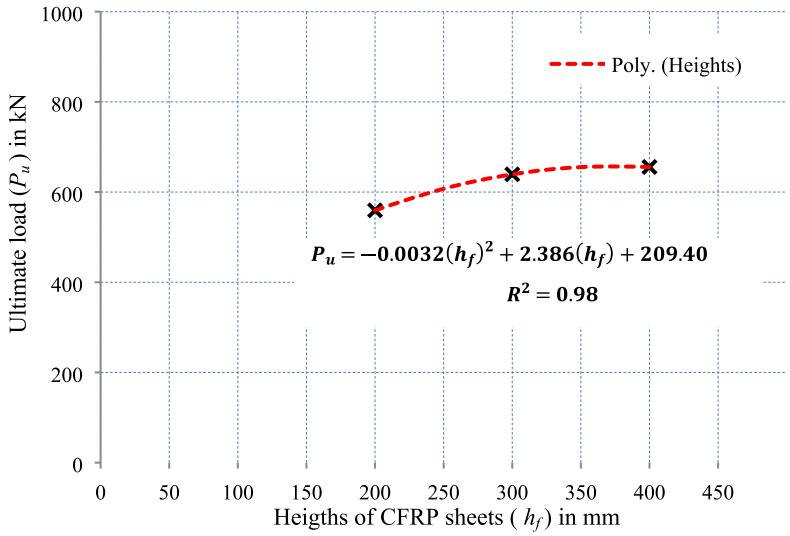
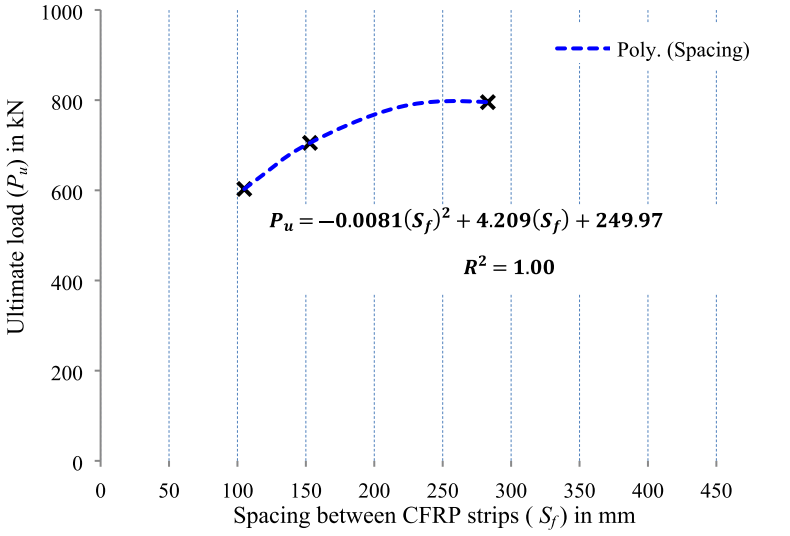


Fig. 10. Crack pattern and mode of failure for all tested ITGs.

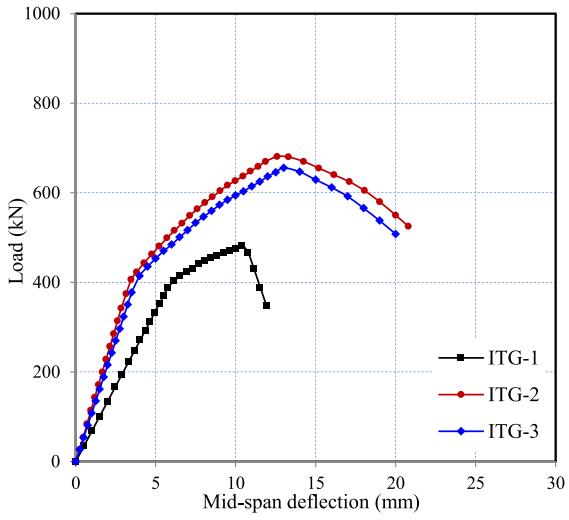


a. Height (h_f) of CFRP vs. the corresponding ultimate load

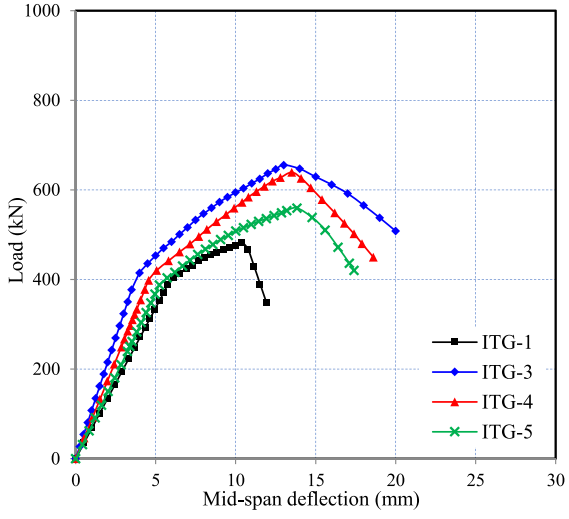


b. Spacing (S_f) of CFRP vs. the corresponding ultimate lo.

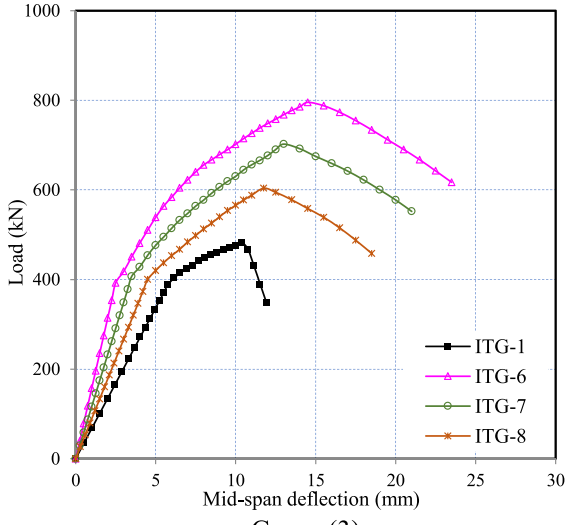
Fig. 11. Effect of height (h_f) and spacing (S_f) of CFRPs on the ultimate load capacity.



a. Group (1)



b. Group (2)



c. Group (3)

Fig. 12. Load-deflection curves for the tested ITGs.

linear up to the hanger cracking load. As the load grows up until failure, deflection has a tendency to rise quickly and deviate from linearity. It is worth mentioning that, according to the experimental parameters, the post-peak behavior of the strengthened specimens differs from that of the control specimen.

To consider significant damage to the specimen, the maximum displacement capacity (δ_{max}) was determined as the load at which the ultimate load experienced a 15% reduction [64]. Column 8 of Table 3 reports the relevant values of displacement for all the test specimens. It can be observed that the displacement capacity (δ_{max}) of the strengthened ITGS is generally higher than that of the reference specimen, with an average value of 60%. Comparing the results obtained for specimens ITG-2 (U-wrapped CFRP) and ITG-3 (side-bonded CFRP) indicates that the strengthening configuration had only a negligible effect on displacement capacity. This finding is interesting not only from a fabrication viewpoint but also from an economic one, as the U-wrapped system needs an CFRPs' area greater than that of the side-bonded system, particularly in large projects. Moreover, the ITGs with discontinuous EB-CFRP strips showed higher displacement capacity (δ_{max}) compared to those with continuous EB-CFRP sheets. The strengthened specimen ITG-6 with three CFRP strips achieved higher displacement than the specimen ITG-3 that was strengthened with a continuous CFRP sheet by 16%.

5.4.2. Initial stiffness response

The initial stiffness (k_i) was calculated as the slope of the load–deflection curve before cracking [65]. Based on the effect of each studied parameter, all strengthened ITGs experienced higher initial stiffness relative to the un-strengthened specimen (ITG-1), as listed in Column 9 of Table 3. For the strengthened specimens ITG-2 and ITG-3 in group (1), the increase in initial stiffness was 76% and 65%, respectively, compared to the control specimen. These results clarify that the initial stiffness was intangibly impacted by using U-wrapped EB-CFRP as opposed to side-bonded sheets. Changing the height of EB-CFRP sheets that were bonded to the web from 200 to 400 mm as obtained in group (2) resulted in an increase in initial stiffness (k_i). Related to the un-strengthened control specimen (ITG-1), the initial stiffness of specimens ITG-3 (h_f = 400 mm), ITG-4 (h_f = 300 mm), and ITG-5 (h_f = 200 mm) increased by about 65%, 27%, and 8%, respectively. Using discontinuous EB-CFRP strips as a strengthening system instead of continuous EB-CFRP sheets generally had a significant enhancement in the initial stiffness of the strengthened ITGs. In particular, the initial stiffness of the strengthened specimen with three EB-CFRP strips (ITG-6) was 153.8 kN/mm, which represents a 35% increase over the strengthened specimen with a continuous EB-CFRP sheet (ITG-3).

5.4.3. Energy dissipation and ductility index

A ductile material is one that can undergo inelastic deformation beyond the initial yielding while still resisting loads. In the current study, two indices were selectively chosen for ductility calculations, namely, energy-based ductility and displacement-based ductility. The first indicator is the energy dissipation index (μ_E), which is defined as the ratio between the energy at failure load (E_{max}) and the energy at yielding load (E_y) [66]. It is worth mentioning that E_{max} and E_y were calculated as the area under the load–deflection curve up to the failure and yielding points, respectively. Columns 11 to 14 of Table 3 list the energy dissipation values determined for the tested ITGs. Overall, the CFRP-strengthened ITGs showed enhanced values of the energy dissipation index (μ_E) compared to the reference specimen (μ_E = 2.08), with a minimum increase of 22% recorded for specimen ITG-5 (μ_E = 2.53). The maximum increase in energy dissipation was reported for specimen ITG-6 (μ_E = 4.24), which is almost twice that of the un-strengthened reference specimen. The discontinuous EB-CFRP strips that were bonded near the loading points showed a better enhancement in energy dissipation compared to those of continuous EB-CFRP sheets. In detail, related to the strengthened specimen ITG-3 (with continuous EB-CFRP sheet), the

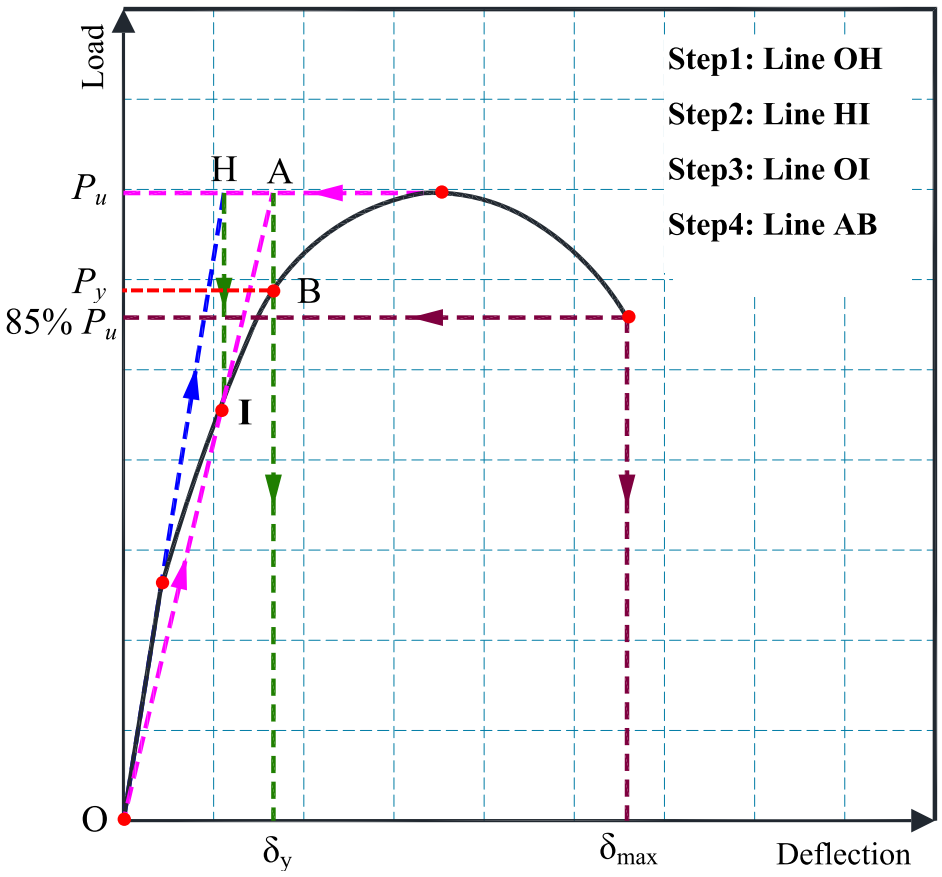


Fig. 13. Definition of yield deflection using general yielding method [67].

energy dissipation indices of specimens ITG-6 (three discontinuous EB-CFRP strips) increased by 25%. Moreover, the EB-CFRP system with bonded heights of 200 mm or 300 mm lost 22% more energy dissipation on average than the system with a bonded height of 400 mm.

The second indicator is the ductility index (μ_D), which is defined as the ratio between the maximum deflection (δ_{max}) relative to that at yielding load (δ_y). For the reader's information, the yield and maximum deflections were calculated using the general yielding method suggested by Baraghith et al. [67]; see Fig. 13. As shown in Columns 15 and 16 of Table 3, the results of the ductility indices for the strengthened ITGs ranged from 1.78 to 2.84, with gains ranging from 21% to 78% compared to the un-strengthened specimen (ITG-1). By analyzing these results, the U-wrapped and side-bonded EB-CFRP configurations display the same results. i.e., the gains in ductility for ITG-2 and ITG-3 are 54% and 48%, respectively. The increase in ductility appears to be sensitive to changes in the heights of the EB CFRP that was bonded to the web (h_f) and the spacing between CFRP strips (S_f). In particular, the ductility indices were 2.37, 1.89, and 1.78 for specimens ITG-3 (h_f = 400 mm), ITG-4 (h_f = 300 mm), and ITG-5 (h_f = 200 mm), respectively. Also, the increases in ductility index were 78%, 66%, and 21% for ITG-6 (S_f = 283 mm), ITG-7 (S_f = 153 mm), and ITG-8 (S_f = 105 mm), respectively, compared to the control specimen. All in all, regarding the ductility response, it can be concluded that the ductility of the strengthened ITGs was noticeably enhanced by using discontinuous EB-CFRP strips (ITG-6, ITG-7, and ITG-8) as opposed to continuous EB-CFRP sheets (ITG-3, ITG-4, and ITG-5).

5.5. Strain response

As depicted in Figs. 8 and 9, strain gauges were used to measure strains at different locations along the studied zone of each specimen: the compressive strain of concrete, the tensile strain of flexural reinforcement, the tensile strain of hanger reinforcement (hanger stirrups), and the tensile strain of the CFRP system. In the event that an electric strain gauge showed erratic behavior that indicated debonding from the reinforcement prior to the failure of the specimen, the data points were removed.

5.5.1. Compressive and tensile flexural strains

The results of the maximum compressive strain in concrete for the tested ITGs are listed in Column 17 of Table 3. The maximum value was observed for ITG-6 (ε_{cmax} = 2712$\mu\varepsilon$), which did not reach the maximum compression strain in flexure (ε_{cu} = 3000$\mu\varepsilon$) according to ACI 318–19 [48]. This ensured that the modes of failure of these specimens were governed by hanger, not flexural failure. In addition, the strain results in Column 18 of Table 3 indicate the effectiveness of the proposed EB-CFRP technique for strengthening ITGs. In other words, the maximum tensile strains of flexural reinforcement measured at failure for the strengthened ITGs were almost more than twice those for the un-strengthened specimen (ITG-1). This indicates that the EB-CFRP strengthening

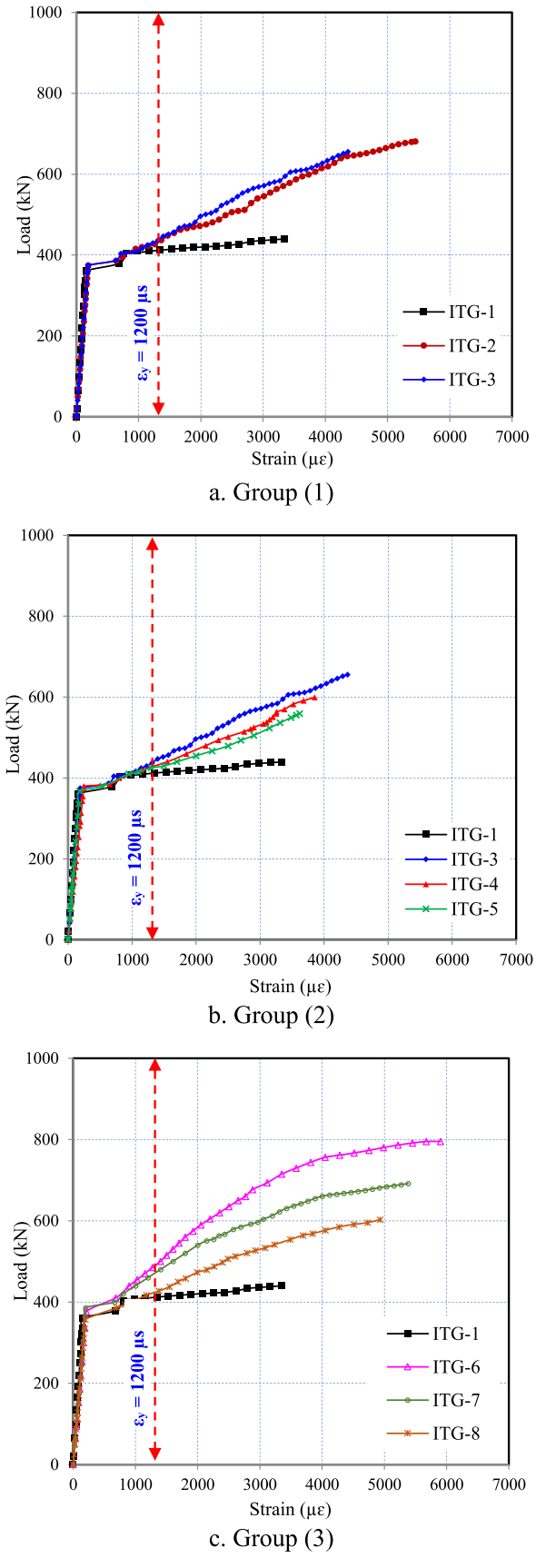


Fig. 14. Load-strain of hanger stirrups for the tested ITGs.

system played a superior role in delaying the failure of the non-ductile hanger by letting the flexural steel move one step closer to the yield region.

5.5.2. Hanger reinforcement strains

The load–strain relationship for the hanger reinforcement of all tested specimens exhibited a bi-linear trend as shown in Fig. 14. The first stage of the load–strain relationship is represented by a straight line beginning at the origin point and continuing along the vertical axis until the first horizontal crack appears between the bottom flange and the web. This behavior means that the hanger stirrups did not originally contribute to the hanger capacity of the ITGs until the first hanger crack was formed. Subsequent to the cracks' spread, the second stage was started by a sudden increase in the strains of hanger stirrups. This sudden jump in strain was a theoretical way to figure out the cracking loads of EB-CFRP-strengthened ITGs. Finally, the relationship prolonged up to the yielding strain of hanger stirrups ($\varepsilon_y = 1200\mu\varepsilon$) and continued to increase up to failure load. As a brief note, the values of the hanger stirrup strains at failure (ε_{hmax}) for the strengthened ITGs were in the range of 3618–5901 με; however, this value is 3342 με for the unstrengthened specimen (ITG-1) as shown in Column 19 of Table 3. In other words, the developed strains for strengthened ITGs increased by an average of 43% compared to the reference specimen. This result confirms that the proposed EB-CFRP system is able to increase the efficiency of internal hanger stirrups and grant enhancements in the ductility performance of hanger failure.

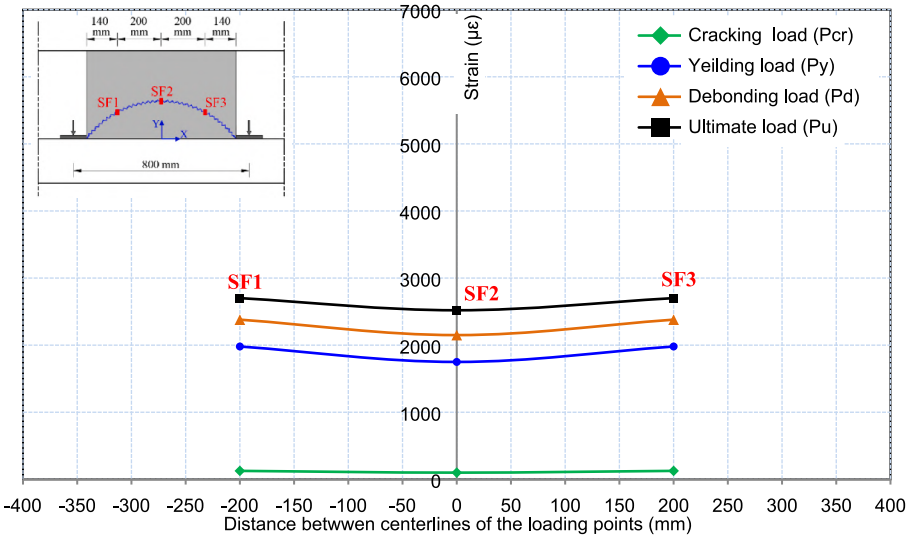
5.5.3. CFRP strain distribution along the hanger failure region

On all CFRPs that crossed the expected hanger crack, electrical strain gauges were mounted in the direction of the fibers. Figs. 15 through 17 show the tensile strain distribution of CFRPs along the distance between the two applied loads at different loading levels (cracking, yielding, debonding, and ultimate loads). It should be emphasized that the yielding load was determined according to the steps mentioned in Fig. 13. By analyzing the relationship for each specimen, corresponding to the cracking load level, the strain distribution is constant over the studied zone, and the maximum recorded strain value approximately equals 180 με, which can be explained by no contribution of the EB-CFRP system to the cracking capacity. In contrast, the strain distributions at other load levels are clearly nonuniform and are close to being parabolic. In other words, the tensile strains developed more quickly in the CFRPs near the loading points than in those close to the mid-span. For example, at the ultimate load level, the tensile strain of the strip in mid-span (SF4) for ITG-8 decreased by 41% compared with the counterpart strip near the applied loads (SF1). Precisely, the most stressed CFRP strips are those that are adjacent to the loading points. Finally, we can say that the best way to strengthen inverted T-girders is to use discontinuous side-bonded EB-CFRP strips near the stringer reactions.

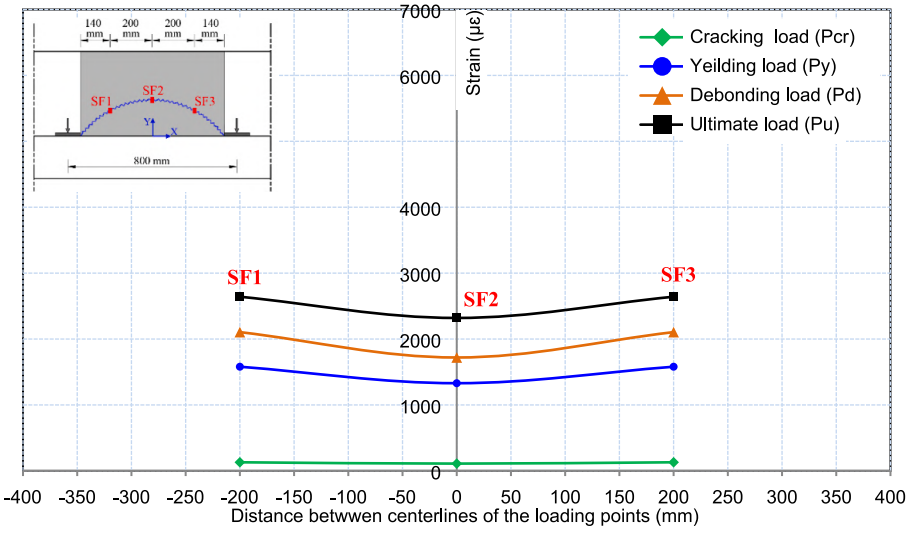
6. Analytical model

6.1. Estimation of the hanger capacity formula for CFRP-strengthened ITGs

Fig. 18 is a systematic sketch of the resistance forces that are generated in CFRP-strengthening RC inverted T-girders (ITGs). From the equilibrium of the forces acting on the hanger failure zone, the proposed hanger capacity (P_{pro}) of the strengthened ITGs comprises three contributions (V_c, V_{sh}, and V_f), as given in Eq. (1). A formula was previously established by Galal and Sekar [59] to determine the resistance produced by the concrete section (V_c); see Eq. (2). This resistance is mainly based on the effective depth (d_f) and the width (b_f) of the bottom flange, as well as the concrete's compressive strength (f_c'). Eq (3) illustrates the resistance of hanger stirrups (V_{sh}), which depends on the area (A_{sh}) and

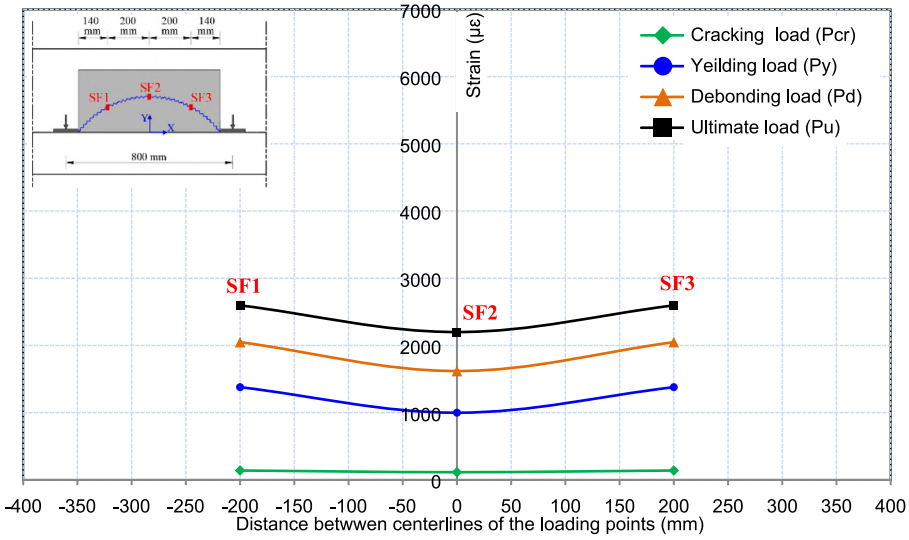


a. Specimen ITG-2

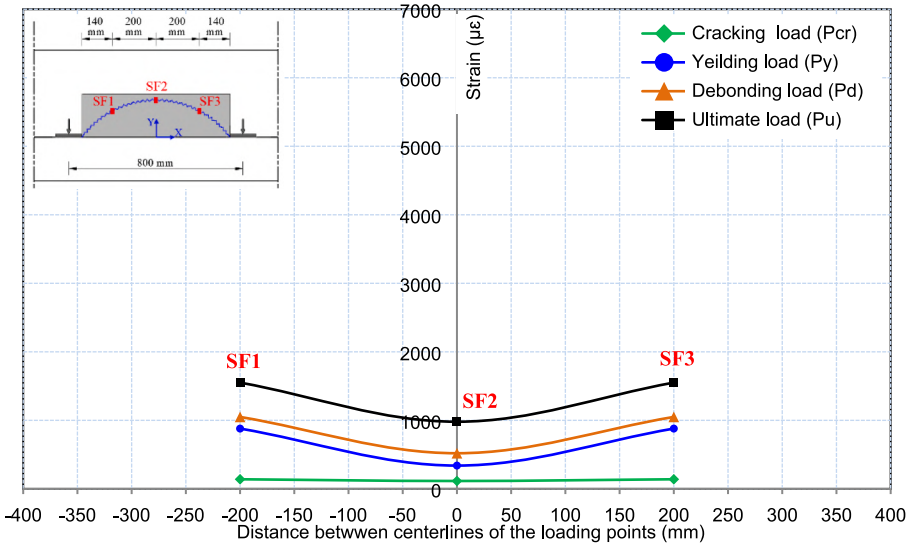


b. Specimen ITG-3

Fig. 15. CFRP strain distribution over mid-span for ITGs in group (1).

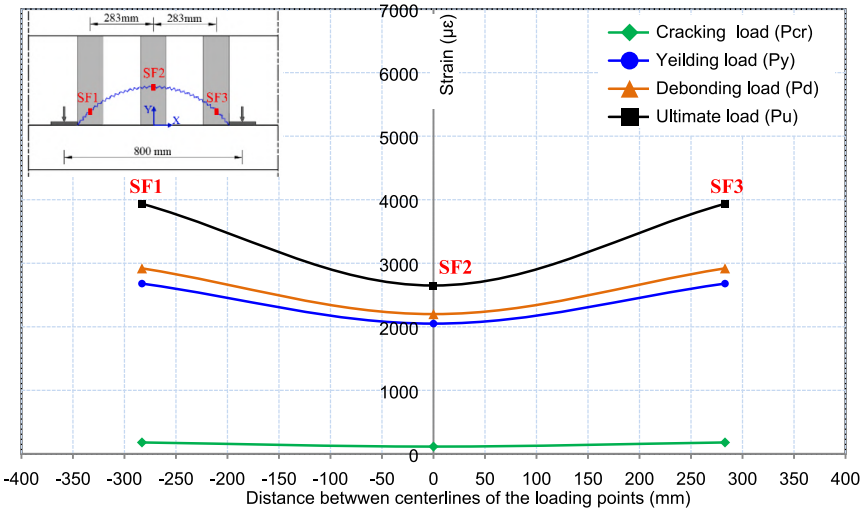


a. Specimen ITG-4

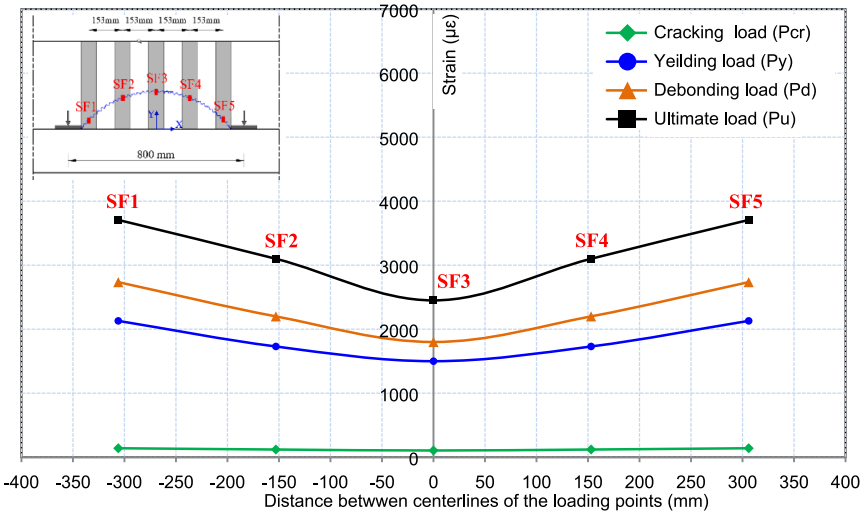


b. Specimen ITG-5

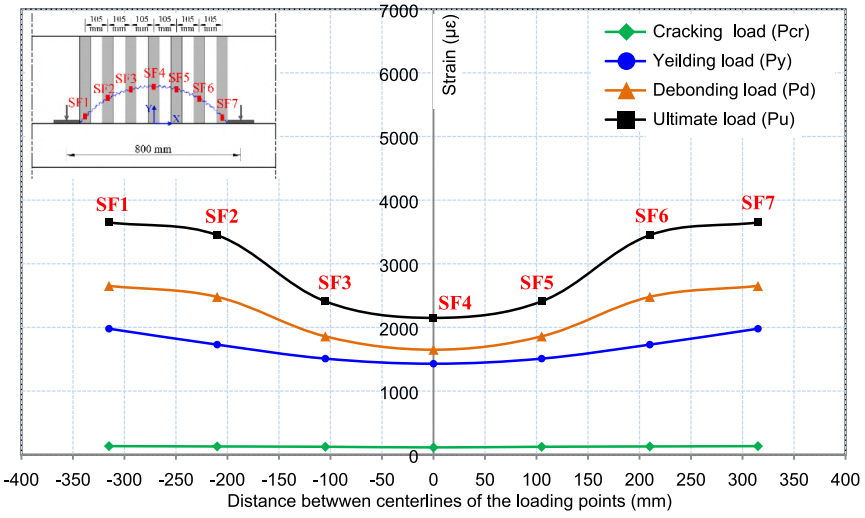
Fig. 16. CFRP strain distribution over mid-span for ITGs in group (2).



a. Specimen ITG-6



b. Specimen ITG-7



c. Specimen ITG-8

Fig. 17. CFRP strain distribution over mid-span for ITGs in group (3).

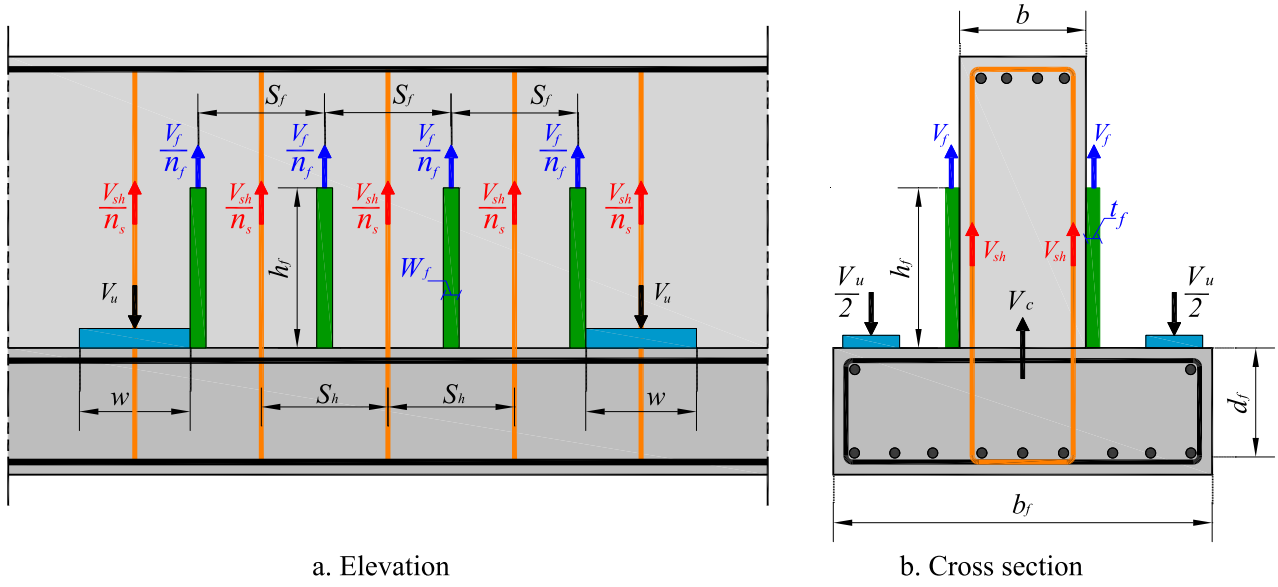


Fig. 18. Systematic sketch of resistance forces that generated in strengthened ITGs.

the spacing (S_h) related to the hanger reinforcement in the studied zone. It is worth mentioning that f_{yh} is the yield strength of hanger reinforcement and w is the width of the loading plate.

$$P_{pro} = 2(V_c + V_{sh} + V_f) \tag{1}$$

$$V_c = 0.33\sqrt{f_c'}\, b_f\, d_f \tag{2}$$

$$V_{sh} = \frac{w + 2d_f}{S_h} f_{yh} A_{sh} \tag{3}$$

The resistance of the EB-CFRP system (V_f) determined by Eqs. (4)–(9) is mainly associated with the effective stress (f_{fe}) of CFRPs, which is defined as the stress concentrations at the concrete-CFRP interface next to the cracks [68–70]. Also, this stress (f_{fe}) depends on the failure mode of the strengthened ITGs (debonding of EB-CFRP sheets or strips). Chen and Teng [71] have already established that Eq. (5) shows the effective stress (f_{fe}) in the EB-CFRPs.

$$V_f = f_{fe} A_f \tag{4}$$

$$f_{fe} = 0.427\,\beta_l \beta_w \sqrt{\frac{E_f \sqrt{f_c'}}{t_f}} \tag{5}$$

where E_f, A_f, and t_f are expressed as the modulus of elasticity, the total area, and the thickness of the CFRP, respectively. Furthermore, β_l indicates the influence of the bond height and β_w reflects the effect of the EB-CFRP-to-concrete width ratio (W_f/S_f), see Eqs. (6) and (7). It should be noted that for a strengthening system with continuous EB-CFRP sheets, the value of $\beta_w = \sqrt{\frac{1}{2}}$ because W_f/S_f equals 1.0 in this case.

$$\beta_l = \begin{cases} 1.0 if \lambda \geq 1.0 \\ \sin\dfrac{\pi\lambda}{4} if \lambda < 1.0 \end{cases} \tag{6}$$

$$\beta_w = \begin{cases} \sqrt{\dfrac{1}{2}} for EB - CFRP sheets \\ \sqrt{\dfrac{2 - (W_f/S_f)}{1 + (W_f/S_f)}} for EB - CFRP strips \end{cases} \tag{7}$$

Where W_f is the width of the EB-CFRP strip, S_f is the perpendicular center-to-center spacing of the EB-CFRP strips, and λ is the normalized bond height ($\lambda = h_{max}/h_e$), which depends on the strengthening configuration (U-wrapped or side-bonded), the number of EB-CFRP plies (n_p), the height of the EB-CFRP sheet that is bonded to the web (h_f), the maximum bond height (h_{max}), and the effective bond height (h_e). The values of h_{max} and h_e are presented in Eqs. (8) and (9), respectively.

$$h_{max} = \begin{cases} h_f for U - wrapped CFRP \\ 0.50 h_f for side - bonded CFRP \end{cases} \tag{8}$$

$$h_e = \sqrt{\frac{n_p E_f t_f}{\sqrt{f_c'}}} \tag{9}$$

6.2. Verification of the proposed model against the experimental results

Table 4 compares the experimental capacities (P_{exp}) with those obtained from the proposed capacities (P_{pro}) to ensure that the proposed model for estimating hanger capacity is accurate. The ratio ranged between 1.01 and 1.08, with a standard deviation of 0.03 and a coefficient of variation (COV) of about 2.88%. This statistical analysis shows that the proposed model can predict the hanger capacities of CFRP-strengthened ITGs with an average error of about 4%. Appendix (A) also includes an example of the predicted hanger capacity for the strengthened ITG-6.

7. Summary and conclusions

This paper examined the hanger capacity and ductility performance

Table 4
Validation of the proposed model against the experimental results.

Specimen No.	Concrete resistance (V_c)				Hanger stirrups resistance (V_{sh})			EB-CFRP sheets or strips resistance (V_f)										Validation results		
	f_c' (MPa)	b_f (mm)	d_f (mm)	V_c (kN)	f_{yh} (MPa)	S_h (mm)	A_{sh} (mm^2)	V_{sh} (kN)	h_f (mm)	W_f (mm)	S_f (mm)	t_f (mm)	n_p	h_e (mm)	h_{max} (mm)	λ	B_l	β_w	f_{fe} (MPa)	V_f (kN)	P_{pro} (kN)	P_{exp} (kN)	P_{exp} /P_{pro}
ITG-1	30.1	600	168	182.5	245	200	100.6	56.2	–	–	–	–	–	–	–	–	–	–	–	–	477.4	482.1	1.01
ITG-2	32.4	600	168	189.3	245	200	100.6	56.2	400	168	–	0.331	1	118.6	400	3.37	1.00	0.707	616	68.5	628.0	680.9	1.08
ITG-3	31.5	600	168	186.7	245	200	100.6	56.2	400	168	–	0.331	1	119.5	200	1.67	1.00	0.707	612	68.1	622.0	655.6	1.05
ITG-4	30.3	600	168	183.1	245	200	100.6	56.2	300	168	–	0.331	1	120.6	150	1.24	1.00	0.707	606	67.4	613.4	639.3	1.04
ITG-5	28.1	600	168	176.3	245	200	100.6	56.2	200	168	–	0.331	1	122.9	100	0.81	0.59	0.707	351	39.0	543.0	559.5	1.03
ITG-6	31.4	600	168	186.4	245	200	100.6	56.2	400	113	283	0.331	2	169.1	200	1.18	1.00	1.069	924	138.2	761.6	795.5	1.04
ITG-7	32.2	600	168	188.8	245	200	100.6	56.2	400	68	153	0.331	2	168.0	200	1.19	1.00	1.038	903	81.3	652.6	702.2	1.08
ITG-8	30.2	600	168	182.8	245	200	100.6	56.20	400	49	105	0.331	2	170.7	200	1.17	1.00	1.022	875	56.8	591.6	603.0	1.02
Average																							1.04
Standard deviation (STDEV.)																							0.03
Coefficient of variation (COV.)																							2.88%

Where, f_c is the concrete's compressive strength for standard cylinder, b_f is the width of the bottom flange, d_f is the effective depth of the bottom flange, V_c is the hanger resistance produced by concrete section, f_{yh} is the yield strength of hanger reinforcement, S_h is the spacing between hanger stirrups, A_{sh} is the area of hanger reinforcement, V_{sh} is the hanger resistance produced by the hanger stirrups, h_f is the height of the EB-CFRPs that is bonded to the web, W_f is the width of the EB-CFRPs, S_f is the perpendicular center-to-center spacing of the EB-CFRPs, t_f is the nominal thickness of the EB-CFRPs, n_p is the number of CFRP plies, h_e is the effective bond height, h_{max} is the maximum bond height, λ is the normalized bond height, β_l indicates the influence of the bond height, β_w reflects the effect of the EB-CFRP-to-concrete width ratio, f_{fe} is the effective stress of the EB-CFRPs, V_f is the hanger resistance produced by the EB-CFRPs, P_{pro} is the proposed hanger capacity for strengthened ITGs, and P_{exp} is the experimental hanger capacity for strengthened ITGs.

of eight third-scale inverted T-girders (ITGs) strengthened with Externally Bonded Carbon Fiber Reinforced Polymers (EB-CFRP). According to the used concrete dimensions, reinforcement details, and the studied parameters, the conclusions drawn from this study are:

- Generally, the EB-CFRP systems exhibited efficient performance in improving the hanger capacity of the strengthened ITGs. Compared to the un-strengthened reference (ITG-1), the strengthened ITGs increased the ultimate load by an average of 37%.
- Regardless of the tested parameters, the adopted strengthening system has remarkably enhanced the obtained energy absorption and the ductility characteristics of all CFRP-strengthened ITGs. The gain in the energy absorption ranged approximately from 22% to 104% relative to the un-strengthened specimen (ITG-1).
- For the same cross-sectional area of EB-CFRP sheets, there is no significant benefit in terms of hanger capacity (5%), or ductility index (6%) derived from using U-wrapped instead of side-bonded configurations.
- Using EB-CFRP sheets with full bonding height equal to web depth (400 mm) was more efficient than for those with 300 or 200 mm, implying there is an interaction between the contribution of CFRP and its debonding heights. This interaction was also verified through capacity component analysis in this study.
- The gain in hanger capacity owing to EB-CFRP discontinuous strips is significantly greater than with CFRP continuous sheets. In other words, the ITGs that were strengthened with discontinuous strips had a 21% higher ultimate load than the ITGs that were strengthened with a continuous EB-CFRP sheet.
- Due to the nonlinearity of the strain distribution on the CFRP over the studied zone, it is recommended that EB-CFRP strips be positioned as close as possible to the loading points.
- An analytical model has been proposed to predict the CFRP contribution to the hanger capacity of strengthened ITGs. The theoretical and experimental results were very close (average error = 4%). But it's important to note that the proposed analytical model shown in this study should also be checked to see how well it works in other situations.

Data availability

The raw data required to reproduce these findings are available only with direct contact through email to the corresponding author. The processed data required to reproduce these findings are available only with direct contact through email to the corresponding author.

Funding

The author(s) received no financial support for the research, authorship, and/or publication of this article.

CRediT authorship contribution statement

Ahmed M. Atta: Supervision, Conceptualization. **Reda N. Behiry:** Conceptualization, Methodology, Formal analysis, Writing – original draft, Writing – review & editing, Investigation, Data curation, Resources. **Mohammed I. Haraz:** Data curation, Resources.

Declaration of Competing Interest

The authors declare that they have no known competing financial interests or personal relationships that could have appeared to influence the work reported in this paper.

Appendix (A)

The resistance generated by the concrete section (V_c)

$$V_c = 0.33\sqrt{f'_c}b_f d_f = 0.33\sqrt{31.4}(600x168) = 186397N = 186.4kN$$

The resistance of web hanger reinforcement (V_{sh})

$$V_{sh} = \frac{w + 2d_f}{S_h} f_{yh} A_{sh} = \frac{(120 + 2*168)}{200}(245x2x50.3) = 56195N = 56.2kN$$

The resistance of EB-CFRP strips (V_f)

$$h_e = \sqrt{\frac{n_p E_f t_f}{\sqrt{f'_c}}} = \sqrt{\frac{2 \times 242000 \times 0.331}{\sqrt{31.4}}} = 169.1mm$$

For side-bonded EB-CFRP strips $\rightarrow h_{max} = 0.50h_f = 0.50 \times 400 = 200mm$

$$\lambda = \frac{h_{max}}{h_e} = \frac{200}{169.1} = 1.18 \geq 1.0 \rightarrow \beta_l = 1.0$$

For side-bonded EB-CFRP strips

$$\beta_w = \sqrt{\frac{2 - (W_f/S_f)}{1 + (W_f/S_f)}} = \sqrt{\frac{2 - (113/283)}{1 + (113/283)}} = 1.069$$

$$f_{fe} = 0.427\beta_l\beta_w\sqrt{\frac{E_f\sqrt{f'_c}}{t_f}} = 0.427 \times 1.0 \times 1.069\sqrt{\frac{242000 \times \sqrt{31.4}}{0.331}} = 924MPa$$

$$V_f = f_{fe}A_f = 924 \times (2 \times 113 \times 2 \times 0.331) = 138241N = 138.2kN$$

The proposed hanger capacity (P_{pro})

$$V_{pro} = 2(V_c + V_{sh} + V_f) = 2\times(186.4 + 56.2 + 138.2) = 761.6\,kN$$

$$P_{exp.} = 795.5\,kN$$

$$\frac{P_{exp.}}{P_{pro}} = \frac{795.5}{761.6} = 1.04$$

References

[1] Muciaccia G, Khorasani M, Mostofinejad D. Effect of different parameters on the performance of FRP anchors in combination with EBR-FRP strengthening systems: A review. Constr Build Mater 2022;354:129181. https://doi.org/10.1016/j.conbuildmat.2022.129181.

[2] Sanginabadi K, Yazdani A, Mostofinejad D, Czaderski C. RC members externally strengthened with FRP composites by grooving methods including EBROG and EBRIG: A state-of-the-art review. Constr Build Mater 2022;324:126662. https://doi.org/10.1016/j.conbuildmat.2022.126662.

[3] Al-Zu'bi M, Fan M, Anguilano L. Advances in bonding agents for retrofitting concrete structures with fibre reinforced polymer materials: A review. Constr Build Mater 2022;330:127115. https://doi.org/10.1016/j.conbuildmat.2022.127115.

[4] ACI Committee 562, 2016. Code Requirements for Assessment, Repair, and Rehabilitation of Existing Concrete Structures and Commentary. American Concrete Institute.

[5] Tena-Colunga A, Hernandez-Marquez O, Archundia-Aranda HI. Strengthening of reinforced concrete prismatic and haunched beams using light jacketing. J Build Eng 2020;32:101757. https://doi.org/10.1016/j.jobe.2020.101757.

[6] Ojaimi MF. Experimental study on shear strengthening of reinforced concrete beams using different techniques of concrete jacketing. Basrah J Eng Sci 2021;2(1):2. https://doi.org/10.33971/bjes.21.2.8.

[7] Abu Maraq MA, Tayeh BA, Ziara MM, Alyousef R. Flexural behavior of RC beams strengthened with steel wire mesh and self-compacting concrete jacketing — experimental investigation and test results. J Mater Res Technol 2021;10:1002–19.

[8] Thermou GE, Papanikolaou VK, Lioupis C, Hajirasouliha I. Steel-Reinforced Grout (SRG) strengthening of shear-critical RC beams. Constr Build Mater 2019;216:68–83. https://doi.org/10.1016/j.conbuildmat.2019.04.259.

[9] Zhang X, Luo Y, Wang L, Zhang J, Wu W, Yang C. Flexural strengthening of damaged RC T-beams using self-compacting concrete jacketing under different sustaining load. Constr Build Mater 2018;172:185–95. https://doi.org/10.1016/j.conbuildmat.2018.03.245.

[10] Hung CC, Chen YS. Innovative ECC jacketing for retrofitting shear-deficient RC members. Constr Build Mater 2016;111:408–18. https://doi.org/10.1016/j.conbuildmat.2016.02.077.

[11] Shadmand M, Hedayatnasab A, Kohnehpooshi O. Strengthening of RC beams using steel plate-fiber concrete composite jackets (finite element simulation and experimental investigation). Int J Eng 2022;35(1):73–92. https://doi.org/10.5829/ije.2022.35.01a.07.

[12] Suman P, Sarath Chandra Kumar B, Ramesh K. Strengthening of RC Beams with M-Sand using external bonding of steel plates. IOP Conf Ser: Mater Sci Eng 2020;912(6):062035.

[13] Qin Z, Tian Y, Li G, Liu L. Study on bending behaviors of severely pre-cracked RC beams strengthened by BFRP sheets and steel plates. Constr Build Mater 2019;219:131–43.

[14] Mhalhal JM, Al-Gasham TS, Jabir HA. New technique to enhance the shear performance of RC deep beams using mild steel plates. International Journal of. Eng Technol 2018;7(4.20):86–94. https://doi.org/10.14419/ijet.v7i4.20.25854.
[15] El-Shafiey T, Atta A. Retrofitting of reinforced concrete beams in shear using external prestressing technique. Mag Concr Res 2012;64(3):201–11. https://doi.org/10.1680/macr.10.00157.
[16] Atta AM, Khalil AEH. Strengthening of RC beams with opening in shear zone using external prestressing technique. Mag Concr Res 2015;67(3):133–44. https://doi.org/10.1680/macr.14.00250.
[17] Atta A, Taman M. Innovative method for strengthening dapped-end beams using an external prestressing technique. Mater Struct 2016;49(8):3005–19. https://doi.org/10.1617/s11527-015-0701-8.
[18] Obaydullah M, Jumaat MZ, Alengaram UJ, ud Darain KM, Huda MN, Hosen MA. Prestressing of NSM steel strands to enhance the structural performance of prestressed concrete beams. Constr Build Mater 2016;129:289–301.
[19] Nawaz W, Elchalakani M, Karrech A, Yehia S, Yang B, Youssf O. Flexural behavior of all lightweight reinforced concrete beams externally strengthened with CFRP sheets. Constr Build Mater 2022;327:126966. https://doi.org/10.1016/j.conbuildmat.2022.126966.
[20] Lim C, Jeong Y, Kim J, Kwon M. Experimental study of reinforced concrete beam-column joint retrofitted by CFRP grid with ECC and high strength mortar. Constr Build Mater 2022;340:127694. https://doi.org/10.1016/j.conbuildmat.2022.127694.
[21] Ghaleh RZ, Mostofinejad D. Behaviour of EBRIG CFRP sheet-concrete joint: Comparative assessment with EBR and EBROG methods. Constr Build Mater 2022;346:128374. https://doi.org/10.1016/j.conbuildmat.2022.128374.
[22] Fayyadh MM, Razak HA. Impact of design parameters and cycles of damage loads on CFRP repair effectiveness of Shear-Deficient RC structures. Constr Build Mater 2022;347:128465. https://doi.org/10.1016/j.conbuildmat.2022.128465.
[23] Liu L, Wan S. Flexural bearing capacity of reinforced concrete beams reinforced with carbon fiber reinforced plastics strips and ultra-high performance concrete layers. International Journal of Building Pathology and Adaptation 2022. https://doi.org/10.1108/ijbpa-04-2022-0056.
[24] Rageh BO, El-Mandouh MA, Elmasry AH, Attia MM. Flexural behavior of RC beams strengthened with GFRP laminate and retrofitting with novelty of adhesive material. Buildings 2022;12(9):1444. https://doi.org/10.3390/buildings12091444.
[25] Wahrhaftig ADM, Rodrigues RB, Carvalho RF, Fortes AS. Strengthening reinforced concrete beams with carbon fiber laminate mounted in a U-shape for static and vibration Purposes. International Journal of Civil Engineering 2022;20(1):27–40. https://doi.org/10.1007/s40999-021-00654-4.
[26] El Ghadioui R, Wagner J, Klein J, Proske T, Curbach M, Graubner CA. RC members with a flexural-strengthening layer of CFRP textile-reinforced concrete under monotonic and cyclic long-term loading. Struct Concr 2022;23(2):939–53. https://doi.org/10.1002/suco.202100452.
[27] Jackson CM, Jacques E, Saatcioglu M. Blast retrofit of one-way reinforced concrete members using externally bonded FRP and FRP anchorage. International Journal of Protective Structures 2022;13(2):209–35. https://doi.org/10.1177/20414196221087347.
[28] Alwash D, Kalfat R, Al-Mahaidi R, Du H. Shear strengthening of RC beams using NSM CFRP bonded using cement-based adhesive. Constr Build Mater 2021;301:124365. https://doi.org/10.1016/j.conbuildmat.2021.124365.
[29] Li X, Deng J, Wang Y, Xie Y, Liu T, Rashid K. RC beams strengthened by prestressed CFRP plate subjected to sustained loading and continuous wetting condition: time-dependent prestress loss. Constr Build Mater 2021;275:122187. https://doi.org/10.1016/j.conbuildmat.2020.122187.
[30] Elsanadedy HM, Al-Salloum YA, Alrubaidi MA, Almusallam TH, Siddiqui NA, Abbas H. Upgrading of precast RC beam-column joints using innovative FRP/steel hybrid technique for progressive collapse prevention. Constr Build Mater 2021;268:121130. https://doi.org/10.1016/j.conbuildmat.2020.121130.
[31] He W, Wang X, Ding L, Wu Z. Efficiency of different BFRP-based strengthening techniques in improving flexural behavior of RC slabs. Constr Build Mater 2021;308:125002. https://doi.org/10.1016/j.conbuildmat.2021.125002.
[32] Shen D, Li M, Kang J, Liu C, Li C. Experimental studies on the seismic behavior of reinforced concrete beam-column joints strengthened with basalt fiber-reinforced polymer sheets. Constr Build Mater 2021;287:122901. https://doi.org/10.1016/j.conbuildmat.2021.122901.
[33] Yang J, Haghani R, Blanksvärd T, Lundgren K. Experimental study of FRP-strengthened concrete beams with corroded reinforcement. Constr Build Mater 2021;301:124076. https://doi.org/10.1016/j.conbuildmat.2021.124076.
[34] Hosen MA, Jumaat MZ, Alengaram UJ, Sulong NR, Islam AS. Structural performance of lightweight concrete beams strengthened with side-externally bonded reinforcement (S-EBR) technique using CFRP fabrics. Compos B Eng 2019;176:107323. https://doi.org/10.1016/j.compositesb.2019.107323.
[35] Shukri AA, Hosen MA, Muhamad R, Jumaat MZ. Behaviour of precracked RC beams strengthened using the side-NSM technique. Constr Build Mater 2016;123:617–26. https://doi.org/10.1016/j.conbuildmat.2016.07.066.
[36] Milad A, Hussein SH, Khekan AR, Rashid M, Al-Msari H, Tran TH. Development of ensemble machine learning approaches for designing fiber-reinforced polymer composite strain prediction model. Eng Comput 2022;38(4):3625–37. https://doi.org/10.1007/s00366-021-01398-4.
[37] Wakjira TG, Ebead U, Alam MS. Machine learning-based shear capacity prediction and reliability analysis of shear-critical RC beams strengthened with inorganic composites. Case Stud Constr Mater 2022;16:e01008.
[38] Su M, Zhong Q, Peng H, Li S. Selected machine learning approaches for predicting the interfacial bond strength between FRPs and concrete. Constr Build Mater 2021;270:121456. https://doi.org/10.1016/j.conbuildmat.2020.121456.
[39] Basaran B, Kalkan I, Bergil E, Erdal E. Estimation of the FRP-concrete bond strength with code formulations and machine learning algorithms. Compos Struct 2021;268:113972. https://doi.org/10.1016/j.compstruct.2021.113972.
[40] Chen SZ, Feng DC, Han WS, Wu G. Development of data-driven prediction model for CFRP-steel bond strength by implementing ensemble learning algorithms. Constr Build Mater 2021;303:124470. https://doi.org/10.1016/j.conbuildmat.2021.124470.
[41] Chen SZ, Zhang SY, Han WS, Wu G. Ensemble learning based approach for FRP-concrete bond strength prediction. Constr Build Mater 2021;302:124230. https://doi.org/10.1016/j.conbuildmat.2021.124230.
[42] Gómez J, Barris C, Jahani Y, Baena M, Torres L. Experimental study and numerical prediction of the bond response of NSM CFRP laminates in RC elements under sustained loading. Constr Build Mater 2021;288:123082. https://doi.org/10.1016/j.conbuildmat.2021.123082.
[43] Mukhtar FM, Shehadah ME. Experimental verification of 2-and 3-D numerical models for bond-slip behavior of CFRP-concrete. Constr Build Mater 2021;287:122814. https://doi.org/10.1016/j.conbuildmat.2021.122814.
[44] Elsanadedy HM, Abbas H, Almusallam TH, Al-Salloum YA. Hybrid UHPC/NSM CFRP strips vs. traditional systems for flexural upgrading of RC beams-experimental and FE study. Compos Struct 2021;261:113291. https://doi.org/10.1016/j.compstruct.2020.113291.
[45] Lee H, Cho D, An Z, Chung W. Composite behavior of steel I-girders connected to inverted-T bent cap. Int J Steel Struct 2014;14(4):711–21. https://doi.org/10.1007/s13296-014-1203-1.
[46] Mirza SA, Furlong RW. Design of reinforced and prestressed concrete inverted T beams for bridge structures. PCI J 1985;30(4):112–36. https://doi.org/10.15554/pcij.07011985.112.136.
[47] American Association of State Highway and Transportation Officials (AASHTO), "AASHTO LRFD Bridge Design Specification, Customary U.S. Units, 9th Edition," Washington, DC, 2020.
[48] ACI Committee 318 (2019). Building Code Requirements for Structural Concrete (ACI 318-19) and Commentary (ACI 318R-19). American Concrete Institute, Farmington Hills, MI, 519 ppfv.
[49] PCI design handbook precast and pre-stressed concrete. Chicago, Illinois 60606; 2006. 736pp.
[50] Mirza SA, Furlong RW. Strength criteria for concrete inverted T-girders. J Struct Eng 1983;109(8):1836–53. https://doi.org/10.1061/(asce)0733-9445(1983)109:8(1836).
[51] Garber DB, Varney NL, Gómez EF, Bayrak O. Performance of ledges in inverted-T beams. ACI Struct J 2017;114(2):487. https://doi.org/10.14359/51689451.
[52] BSI, B.S., 8110-1: 1997, ". Structural use of concrete–Part 1: Code of practice for design and construction.
[53] Committee ACI. Building Code Requirements for Structural Concrete (ACI 318–02) and Commentary. American Concrete Institute; 2002.
[54] American Association of State Highway and Transportation Officials, "AASHTO LRFD Bridge Design Specifications and Commentary," 4th Edition, Washington, D. C., 2007.
[55] ECP 203-2003: Egyptian Code of Practice for Design and Construction of Reinforced Concrete Structures, ECP203-2003, Housing and Building National Research Center, Egypt.
[56] Kim YJ, Alqurashi A. Torsion of carbon fiber-reinforced polymer-strengthened inverted T-beams under combined loading. ACI Struct J 2022;119(1):27–40. https://doi.org/10.14359/51730532.
[57] Park SH, Cui J, Mander JB, Terzioglu T, Birely AC, Hurlebaus S. Load balancing external post-tensioning for strengthening existing inverted-T bent caps. Eng Struct 2022;253:113777. https://doi.org/10.1016/j.engstruct.2021.113777.
[58] Hurlebaus, S., Mander, J.B., Birely, A.C., Terzioglu, T., Cui, J. and Park, S.H., 2018. Strengthening of existing inverted-T bent caps–volume 1: preliminary design (No. FHWA/TX-18/0-6893-R1-Vol1, Report 0-6893-R1-Vol1). Texas A&M Transportation Institute.
[59] Galal K, Sekar M. Rehabilitation of RC inverted-T girders using anchored CFRP sheets. Compos B Eng 2008;39(4):604–17. https://doi.org/10.1016/j.compositesb.2007.09.001.
[60] ASTM C39/C39M - 21, Standard Test Method for Compressive Strength of Cylindrical Concrete Specimens, ASTM International, 2021; www.astm.org.
[61] ASTM A615/A615M-16, "Standard specification for deformed and plain carbon steel bars for concrete reinforcement." ASTM International, 2016; www.astm.org.
[62] Sika. https://egy.sika.com.
[63] ACI Committee 440.2R-17, 2017. Guide for the Design and Construction of Externally Bonded FRP Systems for Strengthening Concrete Structures. https://doi.org/10.14359/51700867.
[64] Eslami A, Moghavem A, Shayegh HR, Ronagh HR. Effect of FRP stitching anchors on ductile performance of shear-deficient RC beams retrofitted using FRP U-wraps. Structures 2020;23:407–14.
[65] Khalil AEH, Etman E, Atta A, Baraghith A, Behiry R. The effective width in shear design of wide-shallow beams: a comparative study. KSCE J Civ Eng 2019;23(4):1670–81. https://doi.org/10.1007/s12205-019-0830-7.
[66] Afefy HM, Baraghith AT, Mahmoud MH. Retrofitting of defected reinforced-concrete cantilever slabs using different techniques. Mag Concr Res 2020;72(14):703–19. https://doi.org/10.1680/jmacr.18.00340.
[67] Baraghith AT, Mansour W, Behiry RN, Fayed S. Effectiveness of SHCC strips reinforced with glass fiber textile mesh layers for shear strengthening of RC beams:

Experimental and numerical assessments. Constr Build Mater 2022;327:127036. https://doi.org/10.1016/j.conbuildmat.2022.127036.
[68] Phan-Vu P, Tran DT, Pham TM, Dang TD, Ngo-Huu C, Nguyen-Minh L. Distinguished bond behaviour of CFRP sheets in unbonded post-tensioned reinforced concrete beams versus single-lap shear tests. Eng Struct 2021;234:111794. https://doi.org/10.1016/j.engstruct.2020.111794.
[69] Vo-Le D, Tran DT, Pham TM, Ho-Huu C, Nguyen-Minh L. Re-evaluation of shear contribution of CFRP and GFRP sheets in concrete beams post-tensioned with unbonded tendons. Eng Struct 2022;259:114173. https://doi.org/10.1016/j.engstruct.2022.114173.
[70] Mhanna HH, Hawileh RA, Abdalla JA. Comparative analysis of design guidelines for FRP contribution to shear capacity of strengthened RC beams. Procedia Struct Integrity 2022;37:359–66. https://doi.org/10.1016/j.prostr.2022.01.096.
[71] Chen JF, Teng JG. Shear capacity of FRP-strengthened RC beams: FRP debonding. Constr Build Mater 2003;17(1):27–41. https://doi.org/10.1016/s0950-0618(02)00091-0.